

Development of an optimal estimation retrieval scheme for Raman lidar systems

A.C. Povey

Supervisors: R. G. Grainger, D. Rees
Word Count 10,161 (12,264 with appendices)

Summary of acronyms

ABC	Attenuated backscatter coefficient
AERONET	Aerosol robotic network
AOT	Aerosol optical thickness
CUV	Chilbolton ultraviolet Raman lidar
FOV	Field of view
LIDAR	Light detection and ranging
PBL	Planetary boundary layer
PMT	Photomultiplier tube
RACHEL	Robust and compact hybrid environmental lidar
SNR	Signal-to-noise ratio

Summary of mathematical symbols used in main text

Symbol	Description	Units
R	Range from instrument	m
z	Vertical height above the instrument	m
c	Speed of light in vacuum	m s^{-1}
t	Delay between firing the laser and a measurement	s
λ	Wavelength; the subscripts L , X , and N_2 indicate the wavelength of the laser radiation, radiation Raman scattered by a species X , and Raman scattered by nitrogen, respectively	m
$P(\lambda, R)$	Power of laser-induced scattering detected at a range R and wavelength λ	W
$J(\lambda, R, \mathbf{r})$	Laser-induced spectral radiance at a point \mathbf{r} in the plane perpendicular to the telescope axis and range R	W m^{-2}
$q(\lambda, R, \mathbf{r})$	Probability that radiation emanating from a point (R, \mathbf{r}) will be observed by the detector	—
$dA(R, \mathbf{r})$	Unit area at \mathbf{r} in the plane perpendicular to the telescope axis and range R	m^2
A_0	Area of the primary telescope mirror	m^2
$\mathcal{T}(\lambda, R)$	Transmission of the air column between the telescope and a range R at wavelength λ	—
$\eta(\lambda)$	Fraction of energy incident on the telescope at λ that is detected	—
$\xi(R, \mathbf{r})$	Probability that a photon from position (R, \mathbf{r}) reaches the detector, based on geometrical considerations	—
$\beta(\lambda, \lambda_L, R)$	Volume backscattering coefficient; the subscripts m and a denote its molecular and aerosol components, respectively	$\text{m}^{-1} \text{ sr}^{-1}$

Symbol	Description	Units
$I(R)$	Laser irradiance	W m^{-2}
$\psi(R, \mathbf{r})$	Laser beam shape, the fraction of laser irradiance at a position (R, \mathbf{r})	—
$N_x(R)$	Number density of a species X	m^{-3}
$A_L(R)$	Laser cross-sectional area	m^{-2}
$O(R, \epsilon)$	Overlap function, which can be parametrised by ϵ	—
$A(R, \epsilon)$	Effective area	m^{-2}
$ \frac{d\sigma}{d\Omega} _{\pi, \lambda_L, \lambda, X}$	Differential cross-section for species X to backscatter at λ light of wavelength λ_L	$\text{m}^2 \text{ sr}^{-1}$
τ_L	Duration of laser pulse	s
τ_d	Bin width, the duration over which the detectors integrate a power measurement	s
$E(\lambda, R)$	Energy detected from the range bin ending at R ; the subscripts ‘el’ and ‘ra’ indicate measurements of the elastic and Raman channel, respectively	J
$\alpha(\lambda, r)$	Volume extinction coefficient; the subscripts m and a denote its molecular and aerosol components, respectively	m^{-1}
$E_B(\lambda)$	Detector dark count	J
B	Lidar ratio	sr
k	Lidar Ångstrom coefficient	—
$S(R)$	$\ln\{R^2[E_{\text{el}}(\lambda_L, R) - E_B(\lambda_L)]\}$	—
R_m	Reference range at which the aerosol extinction is known	m
C_x	Raman calibration constant	J m^3
κ	Ansmann coefficient	—
\mathbf{y}	Measurement vector	counts
\mathbf{x}	State vector	
\mathbf{x}_a	<i>A priori</i> state vector	
\mathbf{b}	Forward model parameters	
$\mathbf{F}(\mathbf{x}, \mathbf{b})$	Forward model	counts
$\boldsymbol{\varepsilon}$	Noise vector	counts
\mathbf{K}	$\nabla_{\mathbf{x}} \mathbf{F}(\mathbf{x}, \mathbf{b})$; the subscript \mathbf{b} indicates the derivative with respect to the components of \mathbf{b} instead	
$\mathbf{S}_{\varepsilon, a, y, b}$	Error covariance of measurement and forward model, <i>a priori</i> , measurement, and forward model parameters, respectively	
$\hat{\mathbf{x}}$	Maximum <i>a posteriori</i> solution	
$n(\lambda, R)$	Photon counts detected from the range bin ending at R ; the subscripts el and ra indicate measurements of the elastic or Raman channel, respectively	counts

Symbol	Description	Units
$n_B(\lambda)$	Detector dark count	counts
$v(R)$	Functions summarising terms of the forward model independent of the retrieval	
h	Planck's constant	J s
$C_{\text{el,ra}}$	Forward model calibration constants	
ρ_i	State vector range coordinate	m
$S_H(\rho)$	Halldórsson S function	m^4
R_T	Radius of the primary mirror of the telescope	m
R_o	Radius of the secondary mirror of the telescope	m
$w(R)$	Half-width of the laser beam at range R	m
$\mathcal{A}(r_1, r_2; \mu)$	Area of overlap between two circles, radii r_1 and r_2 , with distance μ between their centres	m^2
R_a	Radius of the detector aperture	m
f	Focal length of the telescope	m
Δ	Displacement of the detector aperture from the telescope's focal plane	m
δ	Distance between telescope axis and laser pupil	m
$\phi_{\parallel, \perp}$	Angle between the axes parallel or perpendicular to the plane defined by the telescope axis and laser pupil, respectively	rad
τ	Dead time of a PMT	s
n_0	Number of laser shots averaged to form a profile	—
N	Atmospheric number density	m^{-3}
p	Air pressure	Pa
T	Air temperature	K
k_B	Boltzmann's constant	J K^{-1}
$\sigma_R(\lambda)$	Rayleigh cross-section	m^2
M	Molar mass of dry air	kg mol^{-1}
N_A	Avagadro's constant	mol^{-1}
g	Acceleration due to gravity	m s^{-1}
\mathcal{T}_∞	Aerosol optical thickness of calibration atmosphere	—

Acknowledgements This work is supported by a NERC CASE studentship with Hovemere Ltd. and would not be possible without the support of all the staff there, especially Andrew Page. Without the organisational assistance of Warwick Clifton, RACHEL would never have made it on the roof and without the enthusiasm of David Howell, I'd have never have gotten through the paperwork. The continued IT assistance, advice, and spare parts of Mark Munro and Russell Jones are vital to the operations in Oxford. I am indebted to Duncan Constable for all his mechanical help, Graham Sillman for his guidance with the crane lift, Sarah Calcutt for continuing to juggle the beast that is my expense accounts, Jonathan Storey for his invaluable instruction, Clive Leonard for assistance with the measurements in 2010, and to everyone at the Chilbolton Observatory and their spanners. Finally, thanks to Dan Peters for his endless advice, guidance, assistance, and general tolerance throughout this research.

1 Introduction

Active observation of variations in the scattering properties of the atmosphere have been performed since the 1930's by photographing the beam of a searchlight [Hulbert, 1937]. With the development of radar, the concept of using a pulsed light source to determine the range to a target from the light's time-of-flight was applied to the measurement of cloud base height, after which the technique came to be known as lidar (Light Detection And Ranging). The development of the photomultiplier tube (PMT) enabled more accurate, continuous measurements [Friedland et al., 1956], but it was with the advent of the Q-switched laser that the technique began to be widely exploited. The smaller beam divergence and higher pulse energy afforded by a laser beam enabled observations to much greater heights over shorter time scales, allowing researchers to probe the structure and evolution of the atmosphere in unprecedented detail [Collis, 1966]. Since then, improvements in technology and greater usage of the spectral properties of the atmosphere have ensured the technique remains virtually unrivalled in its resolution of atmospheric variations [Amodeo et al., 2009].

A basic lidar system comprises of a pulsed laser beam directed into the atmosphere, observed by a telescope. The telescope is focused onto a system of filters, dichroics, and/or interferometers to separate the light into channels by its polarisation and wavelength, as required, which are measured by PMTs. The range to the scattering centre is given by $R = \frac{1}{2}ct$, where c is the speed of light and t is the delay since the emission of the pulse. Lidar profiles span several orders of magnitude as the received signal attenuates with the square of the range from the instrument. Multiple detectors and/or telescopes can be used to observe the full range of the profile and monitor different regions of the atmosphere reliably. In order to overcome noise, profiles can be averaged over seconds, minutes, or hours, depending on the application and conditions.

The most widespread usage of meteorological lidar currently are as ceilometers — single-wavelength systems from which cloud base and planetary boundary layer (PBL) height are determined from observations at the transmitted wavelength (known as the elastic return as the photons are only scattered elastically). These systems, though technically simple, present distinct challenges when attempting to quantitatively characterise the atmosphere as they make only one measurement at each height to characterise a complex system.

In order to better constrain the problem, more advanced lidar systems make several measurements. For example:

- Polarisation lidar monitors the depolarising properties of the atmosphere on the laser beam. This gives an indication of the degree of sphericity of the aerosol particles and can be useful in distinguishing clouds from aerosols;
- Differential absorption lidar (DIAL) transmits two similar wavelengths of light — one on a significant absorption feature of a gas under investigation and another away from this feature. Such systems have been used to monitor trace gas distributions since the 1970's [Grant, 1991];
- Raman lidar isolates scattering from a particular species by observing the strongest line of its Raman spectrum. As the cross-section for Raman scattering is several orders of magnitude smaller than that for elastic scattering, such systems require a high degree of optical blocking to prevent

cross-talk between the elastic and inelastic channels;

- Doppler lidar measures the frequency shift of the backscattered light to monitor wind speeds along the beam line. This provides an insight into turbulent mixing in the surface layer and a direct, physical measure of PBL height;
- High spectral resolution lidar utilises the fact that molecular scattering is Doppler broadened by thermal motions of air molecules whilst aerosol scattering is negligibly broadened due to the greater mass of the aerosol particles. Using high resolution optics, the two signals can be separated.

Numerous methods of analysis for lidar data have been developed for a variety of applications. These generally require assumptions about the composition of the aerosol under observation and few give a rigorous derivation of the errors produced, most frequently just propagating the Poisson statistics of photon counting through the calculations. To avoid these difficulties, this report develops an optimal estimation retrieval scheme for Raman lidar systems. Such a scheme can be adapted to include as little calibration data is available and returns rigorously derived estimates of the resulting errors. Data retrieved from this scheme could then be more readily compared to and combined with other data sources, increasing the value of lidar data in the study of aerosol and clouds.

This is important as, with the increase in the global mean density of aerosols, their impact on the global energy budget becomes increasingly important [IPCC, 2007]. A significant and poorly understood component of this relates to the aerosol's interactions with clouds [Lohmann and Feichter, 2005]. These interactions have been investigated using satellite observations, but require the assumption that cloud and aerosol properties can be averaged over several days and tens of kilometres [Bulgin et al., 2008; Koren et al., 2005]. Lidar is limited to investigating a particular location, but can resolve the interactions at a scale more fundamental to the process expected to be involved, complementing satellite measurements across the globe.

This report contains five sections and five appendices. Section 2 briefly summarises the existing algorithms for analysing lidar data. Section 3 outlines the optimal estimation retrieval scheme devised and the current method for describing an instrument. The application of this scheme to both simulated and real data is given in Section 4, with conclusions and plans for future work presented in Section 5. The appendices contain detailed derivations of the results used throughout this report that are not required for a reasonable understanding of the concepts.

2 Laser remote sensing

2.1 The lidar equation

The physics behind a lidar measurement is, to first order, fairly straightforward, as summarised in figure 1, and are almost universally summarised as a single lidar equation. Its derivation that follows is adapted from that in Measures [1992, Chapter 7].

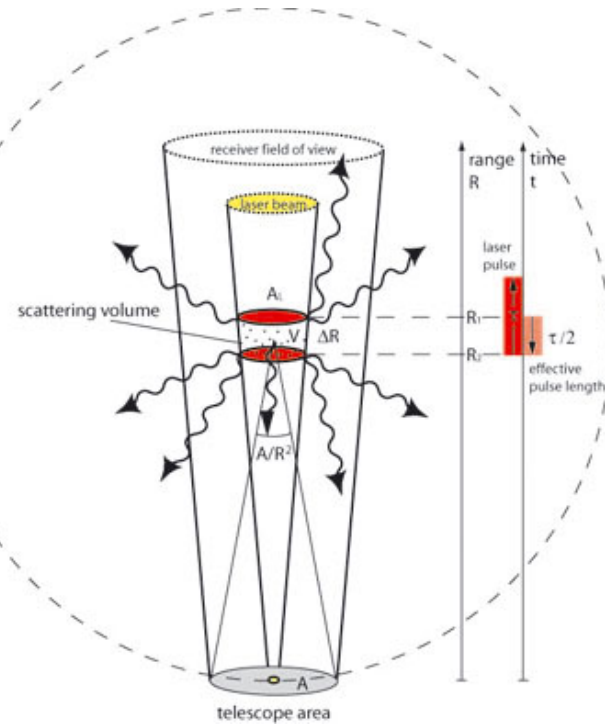


Figure 1: Schematic of lidar backscattering, showing a parcel of air scattering the incident laser energy. A fraction of this falls within the telescope's FOV. [Image credit: Leibniz Institute for Tropospheric Research (accessed Aug. 2010), <http://lidar.tropos.de/en/research/lidar.html>.]

For a pulsed, monostatic lidar, the power received on the wavelength interval $(\lambda, \lambda + \Delta\lambda)$ from the parcel of air in the range interval $(R, R + \Delta R)$ away from the instrument can be written as,

$$\Delta P(\lambda, R) = \int J(\lambda, R, \mathbf{r}) \Delta\lambda \Delta R q(\lambda, R, \mathbf{r}) dA(R, \mathbf{r}), \quad (2.1)$$

where dA represents unit area at the position \mathbf{r} in the plane at range R from the instrument; J describes the laser-induced spectral radiance per unit range at wavelength λ from a point (R, \mathbf{r}) incident on the receiver; and q describes the probability that the radiation emanating from (R, \mathbf{r}) will be observed by the detector.

The detectors are gated such that observations in a given height bin begin at a time t after the laser was fired. The leading edge of the laser pulse takes $t = 2R/c$ to propagate to a range R and back to the detector. The power received at this instant is,

$$P(\lambda, t) = \int_0^{R=ct/2} dR \int_{\Delta\lambda} d\lambda \int J(\lambda, R, \mathbf{r}) p(\lambda, R, \mathbf{r}) dA(R, \mathbf{r}). \quad (2.2)$$

The probability q describes the fraction of energy that, after scattering, is

transmitted into the telescope and then detected. This is written as,

$$q(\lambda, R, \mathbf{r}) = \frac{A_0}{R^2} \mathcal{T}(\lambda, R) \eta(\lambda) \xi(R, \mathbf{r}), \quad (2.3)$$

where $\frac{A_0}{R^2}$ is the acceptance solid angle of the receiver; $\mathcal{T}(\lambda, R)$ is the transmittance of the atmosphere over range R , giving the fraction of energy that is not scattered out of the telescope's field of view (FOV) *en route*; $\eta(\lambda)$ gives the fraction of energy incident on the system that is actually detected; and $\xi(R, \mathbf{r})$ describes the probability that a photon from position (R, \mathbf{r}) reaches the detector, based on geometrical considerations.

The spectral radiance J describes the fraction of energy incident on the parcel that is scattered towards the instrument and can be summarised by,

$$J(\lambda, R, \mathbf{r}) = \beta(\lambda_L, \lambda, R, \mathbf{r}) I(R) \psi(R, \mathbf{r}), \quad (2.4)$$

where the laser beam has irradiance I and beam-shape ψ at wavelength λ_L ; and β is known as the volume backscattering coefficient, a sum across the scattering properties of all species in the atmosphere,

$$\beta(\lambda_L, \lambda, R, \mathbf{r}) = \sum_x N_x(R) \left| \frac{d\sigma}{d\Omega} \right|_{\pi, \lambda, x} \mathcal{L}_x(\lambda), \quad (2.5)$$

where N_x is the number density of species X ; $\frac{d\sigma}{d\Omega}$ is the differential cross-section for backscattering at wavelength λ , which is assumed constant over the receiver's acceptance angle; and \mathcal{L}_x is the fraction of scattered radiation in the wavelength interval $(\lambda, \lambda + \Delta\lambda)$ (this term will be neglected). Strictly, this represents the cross-section for any scattering that is observed by the detector, including multiple scattering, but away from dense concentrations of scatterers, this discrepancy can be neglected.

Substituting (2.3) and (2.4) into (2.2) gives,

$$P(\lambda, t) = A_0 \int_0^{R=ct/2} \frac{dR}{R^2} \int_{\Delta\lambda} \eta(\lambda) d\lambda \times \int \beta(\lambda_L, \lambda, R, \mathbf{r}) I(R) \psi(R, \mathbf{r}) \mathcal{T}(\lambda, R) \xi(R, \mathbf{r}) dA(R, \mathbf{r}). \quad (2.6)$$

It is assumed that the spectral spread of both the scattered radiation and the laser is much smaller than the receiver's spectral window, such that variations in wavelength dependant quantities can be ignored, and that the scattering medium is homogeneous over any given cross-section of the laser. Hence,

$$P(\lambda, t) = A_0 \eta(\lambda) \int_0^R \beta(\lambda_L, \lambda, R) \mathcal{T}(\lambda, R) I(R) \frac{dR}{R^2} \times \int \psi(R, \mathbf{r}) \xi(R, \mathbf{r}) dA(R, \mathbf{r}). \quad (2.7)$$

The second integral describes the overlap between the FOV of the telescope and the laser beam at a range R . This is a fairly elaborate function, which is summarised by,

$$\int \psi(R, \mathbf{r}) \xi(R, \mathbf{r}) dA(R, \mathbf{r}) = O(R, \epsilon) A_L(R), \quad (2.8)$$

where $O(R, \epsilon)$ is the known as the overlap function, which can be parametrised by ϵ ; and $A_L(R)$ is the cross-sectional area of the laser beam.

In addition, it is assumed that the laser emits a short rectangular pulse of duration τ_L . This makes the limits of the first integral in (2.7) $c(t-\tau_L)/2$ to $ct/2$. If the pulse is short enough that $R \gg c\tau_L/2$, we can treat the range-dependant parameters as constants and evaluate (2.7),

$$P(\lambda, t) \approx A_0 \eta(\lambda) \beta(\lambda_L, \lambda, R) \mathcal{T}(\lambda, R) I(R) A_L(R) O(R, \epsilon) \frac{c\tau_L/2}{R^2}. \quad (2.9)$$

For such a rectangular pulse, containing total energy E_L ,

$$I(R) = \frac{E_L \mathcal{T}(\lambda_L, R)}{\tau_L A_L(R)}. \quad (2.10)$$

Hence,

$$P(\lambda, t) = E_L \frac{c}{2R^2} A_0 O(R, \epsilon) \eta(\lambda) \beta(\lambda_L, \lambda, R) \mathcal{T}(\lambda, R) \mathcal{T}(\lambda_L, R). \quad (2.11)$$

The detectors do not detect instantaneous power incident upon them, but the total energy over some interval $(t, t + \tau_d)$. Thus, for $R \gg c\tau_d/2$,

$$E(\lambda, R) = \int_{2R/c}^{2R/c+\tau_d} P(\lambda, t) dt, \quad (2.12)$$

$$\approx E_L \frac{c\tau_d}{2R^2} A_0 O(R, \epsilon) \eta(\lambda) \beta(\lambda_L, \lambda, R) \mathcal{T}(\lambda, R) \mathcal{T}(\lambda_L, R) \quad (2.13)$$

Using the Beer-Lambert law, the transmissions can be written in terms of a volume extinction coefficient, $\alpha(\lambda, R)$, to obtain the fundamental lidar equation,

$$\begin{aligned} E(\lambda, R) &= E_L \frac{c\tau_d}{2R^2} A_0 O(R, \epsilon) \eta(\lambda) \beta(\lambda_L, \lambda, R) \\ &\times \exp \left[- \int_0^R \alpha(\lambda, r) + \alpha(\lambda_L, r) dr \right]. \end{aligned} \quad (2.14)$$

The product $A_0 O(R, \epsilon) \equiv A(R, \epsilon)$ is known as the effective telescope area.

2.2 Elastic backscattering

Considering the elastic scattering, when $\lambda = \lambda_L$,

$$\begin{aligned} E_{el}(R) &= E_L \frac{c\tau_d}{2R^2} A(R, \epsilon) \eta(\lambda_L) \beta(\lambda_L, R) \\ &\times \exp \left[-2 \int_0^R \alpha(\lambda_L, r) dr \right] + E_B(\lambda_L), \end{aligned} \quad (2.15)$$

where E_B describes the dark count of the detector. An example profile is shown in figure 2.

This formulation is widely used throughout the lidar community [Argall and Sica, 2003; Fujii and Fukuchi, 2005; Grant, 1991]. However, it neglects the effects of multiple scattering, which can be very significant when viewing high

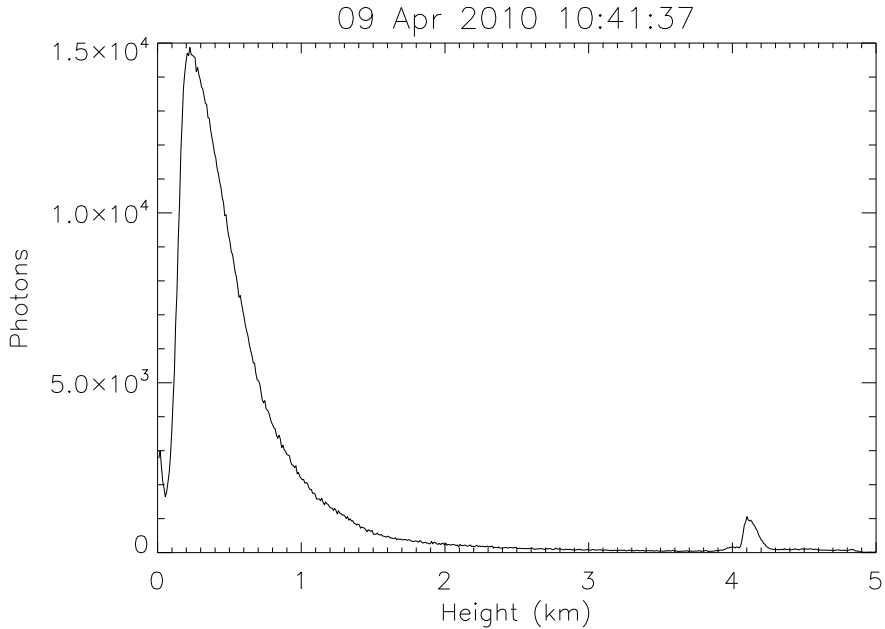


Figure 2: Example of an elastic lidar profile observed by RACHEL from 18,000 laser shots on the morning of the 9th of April, 2010. The shape is mostly dominated by $A(R)/R^2$, with the peak at 4.1 km being a cloud, which is strongly scattering.

concentrations of aerosol, such as a cloud, or when the illuminated area becomes large, such as with space-based observations. A common correction for this, proposed by Platt [1981], is to multiply the aerosol extinction by a multiple scattering factor, commonly denoted η , which is assumed to be known from *in situ* measurements of similar conditions. This can be further developed by separating the atmosphere into layers expected to have similar scattering properties, assigning each its own value of the multiple scattering factor [Vaughan et al., 2004].

Equation (2.15) describes an underconstrained problem with two unknowns but only one measurement at each height. Without additional data, a solution can only be obtained by assuming a relationship between the unknowns α and β . The most common of these, outlined in Klett [1981], assumes that,

$$\beta = B^{-1}\alpha^k, \quad (2.16)$$

where the constants B , known as the lidar ratio, and k , known as the Ångstrom coefficient, are derived from empirical measurements.¹ As the extinction and backscatter coefficients are integrals over the size distributions of gas molecules and aerosols, this assumption is equivalent to stating that the spectral shape and composition of the scatterers are spatially invariant and any variations in backscatter are due solely to variations in scatterer density.

¹This was an extension of the work of Fernald et al. [1972], adding the constant k and deriving a numerically stable solution.

Using this relationship and neglecting the variation of $A(R)$ above some height, equation (2.15) reduces to a Bernoulli equation which is solved in Appendix B.1 to give,

$$\alpha(\lambda_L, R) = \frac{\exp\left[\frac{S(R)-S(R_m)}{k}\right]}{[\alpha(\lambda_L, R_m)]^{-1} + \frac{2}{k} \int_z^{R_m} \exp\left[\frac{S(r)-S(R_m)}{k}\right] dr}, \quad (2.17)$$

where $S(R) = \ln\{R^2[E_{el}(\lambda_L, R) - E_B(\lambda_L)]\}$ and R_m is a reference range at which the extinction is known.

With sufficient signal, the lidar profile can resolve the upper troposphere and stratosphere where it can generally be assumed that aerosol concentrations are sufficiently low for the scattering to be well described by Rayleigh scattering theory and so can be calculated from temperature and pressure profiles of the atmosphere.

The accurate determination of the lidar ratio, B , is a great challenge for single channel lidars. Generally, standard values are used, using knowledge of the aerosol composition based on the source of the air mass [Nicolae et al., 2007]. However, as shown by figure 3 of Ansmann et al. [1992b], the lidar ratio can vary by up to a factor of five across an atmosphere with a variety of different scatterers. Klett [1985] attempts to avoid this difficulty by producing an empirical model for the variation of β , but obviously the preferred solution is to collect data from more than one channel such that α and β can be determined independently.

Because of these difficulties, it is common in modern lidar studies to forgo the calculation of the fundamental backscatter or extinction and instead report an attenuated backscatter coefficient,

$$\begin{aligned} ABC(R) &= \frac{[E_{el}(\lambda_L, R) - E_B(\lambda_L)]R^2}{E_L A(R, \epsilon)} \exp\left[2 \int_0^R \alpha_m(\lambda_L, r) dr\right], \\ &\propto \beta(\lambda_L, R) \exp\left[-2 \int_0^R \alpha_a(\lambda_L, r) dr\right], \end{aligned} \quad (2.18)$$

where the extinction has been broken down into components due to molecular (Rayleigh) and aerosol scattering,

$$\alpha = \alpha_m + \alpha_a. \quad (2.19)$$

2.3 Raman scattering

To remove the need for an assumption linking extinction and backscatter, additional measurements are required. One such measurement utilises a mechanism known as Raman scattering. Raman scattering is an inelastic molecular scattering process whereby a photon of arbitrary wavelength excites an electron to a different vibrational and/or rotational state, changing the energy (and, therefore, wavelength) of the photon with a well-known spectrum for any given species. Transitions that relax the electron to a lower state are known as anti-Stokes lines and those that raise its state Stokes lines (fig. 3). As atmospheric molecules are generally in the ground state, Stokes lines are most frequently

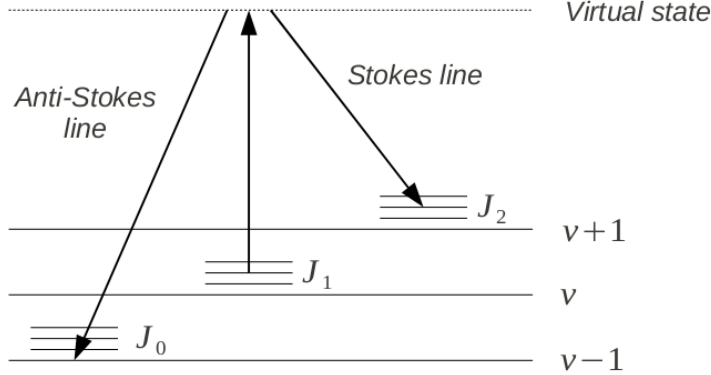


Figure 3: The mechanism of Raman scattering, where a photon excites an electron to a virtual state. This then relaxes back to a different vibrational or rotational level, emitting a photon at a different wavelength. (Image adapted from Measures [1992], p. 105.)

monitored, though anti-Stokes lines can be used to derive the temperature of the gas [Nedeljkovic et al., 1993].

Under these conditions, the sum of equation (2.5) is not necessary and the lidar equation can instead be written as,

$$E_{\text{ra}}(R) - E_B(\lambda_X) = E_L \frac{c\tau_d}{2R^2} A(R, \epsilon) \eta(\lambda_X) N_X(r) \left| \frac{d\sigma}{d\Omega} \right|_{\pi, \lambda_L, \lambda_X, x} \times \exp \left[- \int_0^R \alpha(\lambda_L, r) + \alpha(\lambda_X, r) dr \right], \quad (2.20)$$

$$= \frac{C_x}{R^2} A(R, \epsilon) N_X(R) \times \exp \left[- \int_0^R \alpha(\lambda_L, r) + \alpha(\lambda_X, r) dr \right], \quad (2.21)$$

where λ_X is the wavelength of the Raman scattered radiation from a species X ; $C_x = E_0 \eta(\lambda_L, \lambda_X) \frac{c\Delta t}{2} \left| \frac{d\sigma}{d\Omega} \right|_{\pi, \lambda_L, \lambda_X, x}$; and any possible wavelength dependence of $A(R)$ is neglected. By monitoring a well-mixed gas, such as nitrogen or oxygen, $N_X(r)$ can be calculated from pressure and temperature profiles such that this equation depends only on the extinction.

The most common method of deriving the extinction from a Raman profile was introduced in Ansmann et al. [1990]. It assumes extinction is inversely proportional to wavelength such that,

$$\frac{\alpha_a(\lambda_L, r)}{\alpha_a(\lambda_X, r)} = \left(\frac{\lambda_X}{\lambda_L} \right)^\kappa, \quad (2.22)$$

where $\kappa = 1$ for particles comparable in size to λ and $\kappa = 0$ for larger particles.

By differentiating (2.21) with respect to r , it is shown in Appendix B.2 that,

$$\alpha_a(\lambda_L, R) = \frac{\frac{d}{dR} \left[\ln \frac{N_X(R)}{[E_{\text{ra}}(R) - E_B(\lambda_X)] R^2} \right] - \alpha_m(\lambda_L, R) - \alpha_m(\lambda_X, R)}{1 + (\lambda_L/\lambda_X)^\kappa}. \quad (2.23)$$

This can be substituted into (2.15) to determine the backscatter coefficient. Though this method is obviously preferable in that it determines the two unknowns separately, the calculation of the derivative requires the data to be significantly smoothed in both time and space to give physically sensible results. Various methods of evaluation exist [Turner et al., 2002; Whiteman, 1999] but these involve defining an arbitrary window width for the algorithm to consider, with the width generally increasing with height in some manner.

It should also be noted that by taking the ratio of the Raman profiles for two species, it is possible to eliminate the absorption of the outgoing pulse, giving the ratio of their number densities,

$$\frac{N_x}{N_{N_2}} = C \frac{E_s(\lambda_x, R) - E_B(\lambda_x, R)}{E_s(\lambda_{N_2}, R) - E_B(\lambda_x, R)} \exp \left[\int_0^R \alpha(\lambda_x, r) - \alpha(\lambda_{N_2}, r) dr \right], \quad (2.24)$$

where C is a constant determined by calibration against another measurement of the densities, such as a radiosonde. The exponential can be modelled with standard atmospheres or neglected, depending on the conditions [Guerrero-Rascado et al., 2008]. This is the most common method of measuring humidity with lidar [Ferrare et al., 1995; Goldsmith et al., 1998].

2.4 Summary

The energy observed at the laser wavelength λ_L by a lidar from a range bin of length $c\tau_d$ ending at height R can be expressed in terms of volume extinction and backscatter coefficients, α and β , by,

$$E_{el}(R) = E_L \frac{c\tau_d}{2R^2} A(R, \epsilon) \eta(\lambda_L) \beta(\lambda_L, R) \\ \times \exp \left[-2 \int_0^R \alpha(\lambda_L, r) dr \right] + E_B(\lambda_L).$$

The energy observed due to Raman scattering by a species X at wavelength λ_x is,

$$E_{ra}(R) - E_B(\lambda_x) = E_L \frac{c\tau_d}{2R^2} A(R, \epsilon) \eta(\lambda_X) N_x(r) \left| \frac{d\sigma}{d\Omega} \right|_{\pi, \lambda_L, \lambda_X, x} \\ \times \exp \left[- \int_0^R \alpha(\lambda_L, r) + \alpha(\lambda_x, r) dr \right].$$

3 A joint backscatter and extinction retrieval

3.1 Optimal estimation retrieval

Optimal estimation methods have been successfully applied to satellite retrievals for several years, but have not been widely applied to lidar systems. Volkov et al. [2002] and Shcherbakov [2007] are examples of linearised retrieval schemes, though they do not seem to have been applied beyond the scope of the original papers. A variational method for retrieving ice water path and effective radius in cirrus clouds from coincident spaceborne lidar and radar measurements was

developed in Delanoe and Hogan [2008], though the result is found to be highly dependant on the microphysical assumptions made.

In this work, the intention is to improve existing lidar data products by providing a rigorous method for the inclusion of prior data and additional measurements (such as analogue and photon counting measurements of the same channel) and the calculation of the resulting errors. As such, the retrieved products will be the aerosol extinction and backscatter to provide a direct comparison to existing lidar products. Though it is believed that retrieval of microphysical properties is possible from a two-channel Raman lidar, it is desired in the first instance to avoid assumptions about the microphysical properties of the aerosol and its distribution.

This work uses the retrieval method outlined in Rodgers [2000]. This defines an inverse problem,

$$\mathbf{y} = \mathbf{F}(\mathbf{x}, \mathbf{b}) + \boldsymbol{\varepsilon}, \quad (3.1)$$

which relates the measurement vector, \mathbf{y} , to the state vector, \mathbf{x} , through the forward model, \mathbf{F} , dependant on other, known parameters, \mathbf{b} , with a measurement error $\boldsymbol{\varepsilon}$. For a lidar, the measurement vector describes the number of photons observed in each height bin for each channel; the state vector describes the unknown state of the atmosphere, here summarised by the extinction and backscatter coefficients; and the forward model is a non-linear function which maps a state of the atmosphere onto a measurement a lidar system would make.

The solution, $\hat{\mathbf{x}}$, is sought which has the maximum probability of representing the true state of the atmosphere, given the measurements and any *a priori* information, known as the maximum *a posteriori* solution. This state will minimise some cost function, which enumerates the divergence of the forward modelled from the measured state. Using Bayesian statistics and assuming the probability density functions describing all quantities are Gaussian (or at least symmetric), it is shown in Appendix C that the Levenberg–Marquardt iteration,

$$\mathbf{x}_{i+1} = \mathbf{x}_i + [(1 + \gamma_i) \mathbf{S}_a^{-1} + \mathbf{K}_i^T \mathbf{S}_\varepsilon^{-1} \mathbf{K}_i]^{-1} [\mathbf{K}_i^T \mathbf{S}_\varepsilon^{-1} (\mathbf{y} - \mathbf{F}(\mathbf{x}_i)) - \mathbf{S}_a^{-1} (\mathbf{x}_i - \mathbf{x}_a)],$$

converges towards $\hat{\mathbf{x}}$. In this formulation, $\mathbf{K}_i = \nabla_{\mathbf{x}} \mathbf{F}(\mathbf{x}_i, \mathbf{b})$; \mathbf{S}_ε is the error covariance matrix of the measurement and forward model; \mathbf{x}_a describes the assumed *a priori* state of the atmosphere with associated covariance matrix \mathbf{S}_a ; and γ_i is a constant chosen with each step of the iteration to reduce the cost function.²

Following Rodgers [2000], if the cost function is increased after an iteration, γ_i is increased by a factor of ten. Otherwise, it is reduced by a factor of two. The iteration is considered converged when either the decrease in the cost function is less than some threshold or the change in all elements of the state vector is much less than the error on those values.

3.2 The forward model

3.2.1 Lidar equations

Equations (2.15) and (2.21) describe the energy observed from a range bin R_i due to a single laser shot in terms of the extinction and backscatter coefficients,

²The cost function is defined as $(\mathbf{y} - \mathbf{F}(\mathbf{x}_i))^T \mathbf{S}_\varepsilon (\mathbf{y} - \mathbf{F}(\mathbf{x}_i)) + (\mathbf{x}_i - \mathbf{x}_a)^T \mathbf{S}_a (\mathbf{x}_i - \mathbf{x}_a)$.

α and β . This fundamentally assumes that these coefficients are sensible descriptions of the volume observed. In practice, this implies that over the scale of a bin (order 1 m horizontally and 10 m vertically), the scattering properties of particles are sufficiently homogeneous that their average is physically meaningful. The coefficients are then separated into molecular and aerosol components, as in (2.19), assuming that all scattering beyond that expected from molecular Rayleigh scattering is due to aerosols.

This energy is detected as discrete photons and will generally correspond to less than one photon per bin. Hence, in order to properly resolve this, profiles over several hundred laser shots must be averaged.³ Assuming that the atmosphere does not change significantly during the period averaged, the existing equations can still be applied by redefining E_L as the total laser energy emitted by all averaged shots and dividing by the energy of a photon at λ_L .

For the instruments used in this work, Raman scattering from nitrogen is observed. The centre of the Raman spectrum of nitrogen is shifted 2329.66 cm^{-1} from the laser wavelength with a total cross-section of $3.5 \times 10^{-30}\text{ cm}^2\text{ sr}^{-2}$ [Measures, 1992, table 3.3].

The wavelength dependence of (2.22) is assumed to relate $\alpha_a(\lambda_{N_2}, R)$ and $\alpha_a(\lambda_L, R)$ in the Raman equation. Particle diameters are assumed to be comparable to λ_L , such that $\kappa = 1$ is used throughout. Though this will be a poor model for ice particles, it is assumed that profiles will not consider sufficient heights to observe them in significant quantities.

The number of photons observed from a range bin R_i is therefore given by,

$$n_{el}(R_i) = v_{el}(R_i) [\beta_m(R_i) + \beta_a(R_i)] \exp \left[-2 \int_0^{R_i} \alpha_a(r) dr \right] + n_B(\lambda_L), \quad (3.2)$$

$$n_{ra}(R_i) = v_{ra}(R_i) \exp \left[- \left(1 + \frac{\lambda_L}{\lambda_{N_2}} \right) \int_0^{R_i} \alpha_a(r) dr \right] + n_B(\lambda_{N_2}), \quad (3.3)$$

where n_B is the dark count of the detector; the wavelength dependence of all quantities is dropped for brevity; and, using h as Planck's constant, the functions

³Though the term 'averaged' is used throughout this report for reasons of style, what is actually done is to sum together profiles as this maintains the discrete nature of the data.

$v(R)$ summarise all terms that are independent of the retrieval,

$$\begin{aligned} v_{\text{el}}(R_i) &= \frac{E_L \lambda_L \tau_d}{2R_i^2 h} A(R_i, \varepsilon) \xi(\lambda_L) \exp \left[-2 \int_0^{R_i} \alpha_m(r) dr \right], \\ &\equiv \frac{C_{\text{el}} A(R_i, \varepsilon)}{R^2} \exp \left[-2 \int_0^{R_i} \alpha_m(r) dr \right], \end{aligned} \quad (3.4)$$

$$\begin{aligned} v_{\text{ra}}(R_i) &= \frac{E_L \lambda_L \tau_d}{2R_i^2 h} A(R_i, \varepsilon) \xi(\lambda_{N_2}) \left| \frac{d\sigma}{d\Omega} \right|_{\pi, \lambda_L, \lambda_{N_2}} N_X(R_i) \\ &\quad \times \exp \left[- \left(1 + \frac{\lambda_L}{\lambda_{N_2}} \right) \int_0^{R_i} \alpha_m(r) dr \right], \\ &\equiv \frac{C_{\text{ra}} N_X(R_i) A(R_i, \varepsilon)}{R^2} \exp \left[- \left(1 + \frac{\lambda_L}{\lambda_{N_2}} \right) \int_0^{R_i} \alpha_m(r) dr \right]. \end{aligned} \quad (3.5)$$

These equations are differentiated in Appendix E with respect to α and β to give an analytic expression for \mathbf{K} .

3.2.2 Interpolation

Measurements from below a minimum height of 300 m are neglected in this retrieval as they do not satisfy the assumptions of Section 2.1 and the overlap function varies rapidly in this region. Further, measurements with a signal-to-noise ratio (SNR) of less than one are neglected, as these are not expected to significantly affect the retrieval. This reduces the length of the vector \mathbf{y} to ~ 2000 elements.

The two components of the state vector can be gridded arbitrarily, with the model interpolating each onto the measurement grid. Further, these grids do not necessarily have to be the same or uniform. However, increasing the distance over which correlations are expected in \mathbf{S}_a is equivalent to increasing the length of bins in the state vector. Thus, identical, equally-spaced grids are used as this minimises the number of operations required to calculate \mathbf{K} . It should be noted that the value reported for a height bin gives the top of that bin, such that the first bin represents an assumed uniform surface layer. As this bin will therefore be at least an order of magnitude larger than other bins, it is more likely that the values reported there will be averages over several types of aerosol and should be treated with greater caution in analysis.

In practice, the integrals of equations (3.2) and (3.3) are first evaluated on the grid of the state vector, ρ_j , using a simple trapezium rule integration scheme,

$$\int_0^{\rho_j} \alpha_a(r) dr = \rho_0 \alpha_a(\rho_0) + \sum_{k=1}^j [\alpha_a(\rho_k) + \alpha_a(\rho_{k-1})] [\rho_k - \rho_{k-1}]. \quad (3.6)$$

The backscatter coefficient and this integral are then interpolated onto the measurement axis using the cubic spline method of Section 3.3 of Press et al. [1992], outlined in Appendix D.

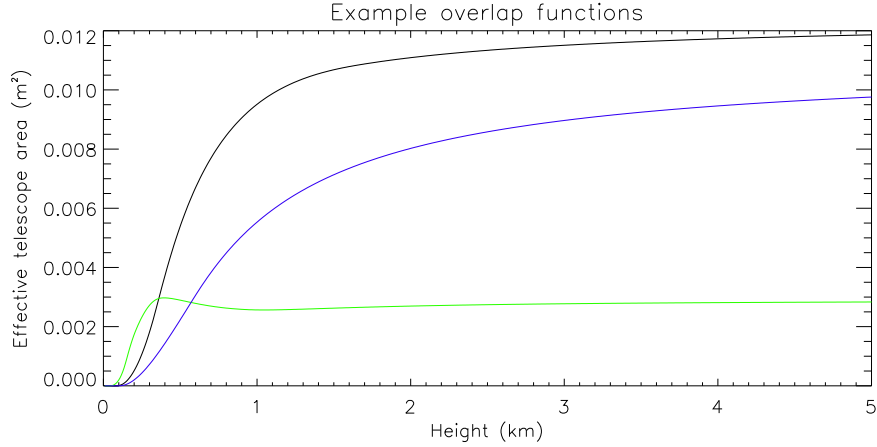


Figure 4: Examples of the effective area model, using the parameters of the RACHEL system (table 2). Alignment parameters summarised in table 5. Black — a perfectly aligned system; Blue — a slight defocusing of the telescope; Green — a greater defocusing of the telescope with non-parallel telescope and laser axis.

3.2.3 Overlap function model

A theoretical parametrisation of the overlap function is presented in Halldórsson and Langerholc [1978], as outlined in Appendix A. That appendix also outlines further evaluation of that solution to improve computational efficiency and accuracy by reducing the ranges over which numerical integration is performed, where possible.

Four parameters are selected to describe the misalignment of the system — the distance between the focal plane and detector aperture, Δ ; the distance between the optical axes of the telescope and laser in the plane of the telescope, δ ; and the angles between these axes in the planes parallel and perpendicular to each, $\phi_{\parallel, \perp}$. Examples of some functional forms are shown in figure 4.

For a lidar system with a telescope with primary mirror of radius R_T and secondary mirror of radius R_o observing a coaxial laser beam of radius $w(R)$ and circular beam profile,

$$A(R, \epsilon) \equiv A_0 O(R, \Delta, \delta, \phi_{\parallel}, \phi_{\perp}) = \left(\frac{\gamma}{\nu}\right)^2 \frac{S_H\left(\frac{\nu}{\gamma}R_T, R\right) - S_H\left(\frac{\nu}{\gamma}R_o, R\right)}{w^2}, \quad (3.7)$$

where,

$$\begin{aligned}
S_H(\rho, R) &= \left\{ \begin{array}{ll} 0, & \alpha + \rho \leq d - w; \\ \pi w^2 \min[\alpha^2, \rho^2], & w + d \leq |\alpha - \rho|; \\ \pi \alpha^2 \rho^2, & \alpha + \rho \leq w - d; \\ \int_{|\alpha-\rho|}^{\alpha+\rho} \sqrt{\Upsilon(\alpha, \rho; \mu)} \mathbb{A}(\mu, w; d) \frac{d\mu}{\mu}, & \alpha + \rho \leq w + d \\ & \text{and } |w - d| \leq |\alpha - \rho|; \\ \int_{d-w}^{\alpha+\rho} \sqrt{\Upsilon(\alpha, \rho; \mu)} \mathbb{A}(\mu, w; d) \frac{d\mu}{\mu}, & \alpha + \rho \leq w + d \\ & \text{and } |\alpha - \rho| < d - w; \\ \mathbb{B} + \int_{w-d}^{\alpha+\rho} \sqrt{\Upsilon(\alpha, \rho; \mu)} \mathbb{A}(\mu, w; d) \frac{d\mu}{\mu}, & \alpha + \rho \leq w + d \quad (3.8) \\ & \text{and } |\alpha - \rho| < w - d; \\ \pi w^2 \mathbb{A}(\alpha, \rho; w + d) & w + d < \alpha + \rho \\ + \int_{|\alpha-\rho|}^{w+d} \sqrt{\Upsilon(\alpha, \rho; \mu)} \mathbb{A}(\mu, w; d) \frac{d\mu}{\mu}, & \text{and } |w - d| \leq |\alpha - \rho|; \\ \pi w^2 \mathbb{A}(\alpha, \rho; w + d) & w + d < \alpha + \rho \\ + \int_{d-w}^{w+d} \sqrt{\Upsilon(\alpha, \rho; \mu)} \mathbb{A}(\mu, w; d) \frac{d\mu}{\mu}, & \text{and } |\alpha - \rho| < d - w; \\ \pi w^2 \mathbb{A}(\alpha, \rho; w + d) + \mathbb{B} & w + d < \alpha + \rho \\ + \int_{w-d}^{w+d} \sqrt{\Upsilon(\alpha, \rho; \mu)} \mathbb{A}(\mu, w; d) \frac{d\mu}{\mu}, & \text{and } |\alpha - \rho| < w - d, \end{array} \right. \\
\mathbb{A}(\mu, w; d) &= \frac{1}{\pi} \left[\mu^2 \cos^{-1} \left(\frac{d^2 + \mu^2 - w^2}{2d\mu} \right) + w^2 \cos^{-1} \left(\frac{d^2 - \mu^2 + w^2}{2dw} \right) \right. \\
&\quad \left. - \frac{\sqrt{\Upsilon(\mu, w; d)}}{2} \right], \\
\mathbb{B} &= \frac{(w - d)^2 - \alpha^2 - \rho^2}{4} \sqrt{\Upsilon(\alpha, \rho; w - d)} \\
&\quad + 2\alpha^2 \rho^2 \tan^{-1} \sqrt{\frac{(w - d)^2 - (\alpha - \rho)^2}{(\alpha + \rho)^2 - (w - d)^2}}, \\
\Upsilon(x, y; z) &= [(x + y)^2 - z^2][z^2 - (x - y)^2], \\
\alpha(R) &= \frac{R_a R}{f \gamma}, \\
\gamma &= 1 + \frac{\Delta}{f}, \\
\nu(R) &= \left| \gamma - \frac{\Delta R}{f^2} \right|, \\
w(R) &= R_L + \phi_L R, \\
d(R) &= \sqrt{(\delta + \phi_{\parallel} R)^2 + (\phi_{\perp} R)^2}.
\end{aligned}$$

Here, all cases are mutually exclusive where not explicitly stated; $\pi \mathbb{A}$ is the area of overlap of two circles, radii μ and w , with centres a distance d apart; $\mathbb{B} = \int_{|\alpha-\rho|}^{w-d} \mu \sqrt{\Upsilon(\alpha, \rho; \mu)} d\mu$; R_a is the radius of the aperture of the detector; f is the telescope's focal length; R_L is the initial radius of the laser beam; and ϕ_L is the divergence of the laser beam. All integrals are evaluated using the Romberg integration scheme outlined in Section 4.3 of Press et al. [1992].

3.2.4 Detector nonlinearity

Finally, the nonlinearity of the PMTs in photon counting mode must be accounted for. There is a finite time, τ , needed for the detector to ramp back up to full voltage after detecting a photon. During this ‘dead’ time, the detector cannot register another count. As reviewed in Whiteman [2003, Appendix B], there are two extremes for this effect:

- Paralysable counters, where an additional photon strike during the dead time extends it a further time τ as it depletes the anode voltage. Assuming the number of photons striking the detector in a given interval is described by a Poisson distribution, the measured number of photons can be written as,

$$n_{\text{meas}} = n_{\text{real}} \exp(-\tau n_{\text{real}}). \quad (3.9)$$

- Non-paralysable counters, where the dead time is a constant. If the detector measures a flux n_{meas} , it was ‘dead’ for a fraction τn_{meas} of the observation such that,

$$\begin{aligned} n_{\text{meas}} &= (1 - \tau n_{\text{meas}}) n_{\text{real}}, \\ &= \frac{n_{\text{real}}}{1 + \tau n_{\text{real}}}. \end{aligned} \quad (3.10)$$

The response of a real detector will lie somewhere between these two extremes. For this model, count rates are assumed to be low enough that the detector acts non-paralysable. To calculate the expected count rate using (3.10), the counts per bin defined in (3.2) and (3.3) must be divided by the number of laser shots, n_0 , and the duration of a range bin, τ_d , giving the forward model equations,

$$n_{\text{el}}^F(R_i) = \frac{n_{\text{el}}(R_i)}{1 + \frac{n_{\text{el}}(R_i)}{n_0} \frac{\tau_{\text{el}}}{\tau_d}}, \quad (3.11)$$

$$n_{\text{ra}}^F(R_i) = \frac{n_{\text{ra}}(R_i)}{1 + \frac{n_{\text{ra}}(R_i)}{n_0} \frac{\tau_{\text{ra}}}{\tau_d}}, \quad (3.12)$$

where $\tau_{\text{el,ra}}$ is the dead time of the detector observing the elastic or Raman profile, respectively.

3.2.5 Error estimates

As the basic measurement made by the lidar is to count photons, the measurement error will be well-described by a Poisson distribution with mean $n(R_i)$. For values above five, this can be well approximated with a normal distribution [Riley et al., 1998], as required for the Levenberg-Marquadt iteration, with variance equal to the mean. Any cross-talk between the channels or bins is currently assumed to be negligible.

The error covariance matrix also summarises the forward model error,

$$\mathbf{S}_\varepsilon = \mathbf{S}_y + \mathbf{K}_b \mathbf{S}_b \mathbf{K}_b^T, \quad (3.13)$$

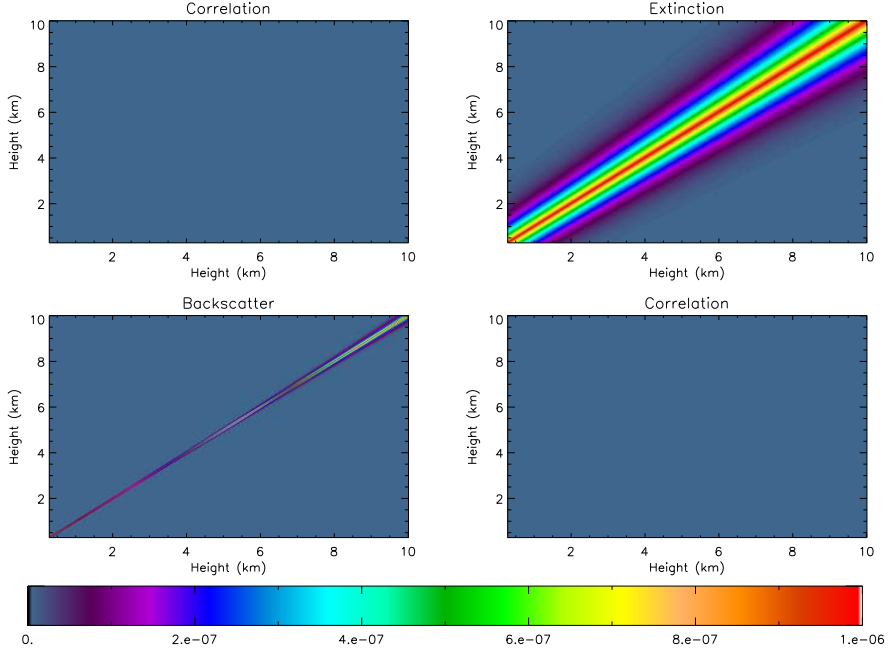


Figure 5: The *a priori* covariance matrix currently used for retrievals, separated into extinction and backscatter components. Correlation between bins decreases exponentially with height. The scale height for backscatter ranges from 10 – 100 m and from 500 – 1000 m for extinction. There is no correlation assumed between the two.

where \mathbf{b} are all parameters of the retrieval not described by \mathbf{y} or \mathbf{x} ;⁴ $\mathbf{K}_\mathbf{b} = \nabla_{\mathbf{x}} \mathbf{F}(\mathbf{x}, \mathbf{b})$; and $\mathbf{S}_\mathbf{b}$ gives the covariance of each element of \mathbf{b} . These have not yet been successfully integrated into the retrieval, such that the algorithm currently underestimates the retrieval error. This is expected to be a small underestimation as these errors should be individually much less than 1%.

The *a priori* state vector would preferably be a climatological average of the extinction and backscatter. However, as regular measurements of these quantities are not currently made at any site used in this study and there have been difficulties in deriving them using existing methods, the *a priori* state is taken to be zero everywhere. Alternative sources of data are being considered, but the *a priori* should not significantly affect the result of the retrieval where there is sufficient information content.

The *a priori* variance is set to be 10^{-6} everywhere for both extinction and backscatter as a weak constraint that does not introduce a shape to the retrieval. Using a larger value for the variance increases the range of states away from the first guess investigated by the algorithm, giving better fits to features not included in that guess, but also permitting unrealistically large variations in the extinction profile. This value needs to be more rigorously determined and should probably be decreased in favour of a more reasonable first guess (such

⁴In full: the dark count and calibration constant of each channel; the laser power; the PMT dead times; the surface pressure; the four parameters of the overlap function; the pressure profile; and the number density profile

as identifying clouds and adding peaks to the first guess profiles).

The correlation between bins is assumed to decay exponentially with their vertical displacement, over a scale height that itself increases with height. This increasingly smooths the profiles as the SNR decreases with height and is paramount to assuming that the vertical extent of air masses increases with height as vertical mixing decreases. The vertical scales chosen were guided by consideration of the width of the averaging kernel of the forward model (without *a priori*) for each channel and are currently set to 10 – 100 m for the backscatter and 500 – 1000 m for the extinction for retrievals from 300 m to 10 km. These values should be reassessed as the algorithm develops to ensure they make best use of the information available.

3.3 Determining the forward model parameters

3.3.1 Meteorology

Knowledge of the state of the atmosphere is needed to determine the number density term in equation (3.5) and the molecular scattering component of the extinction and backscatter. This is commonly deduced from radiosonde measurements [Mattis et al., 2008; Ansmann et al., 1992b; Di Girolamo et al., 1999] or a standard atmosphere [Reagan et al., 1989; Ansmann et al., 1992a; Bockmann et al., 2004]. For intensive measurement campaigns, it is possible to launch radiosondes from the same site as the lidar to obtain the most representative atmospheric profiles. For continuous campaigns, as in this work, such measurements are prohibitively expensive. Instead, regular sonde launches performed at a nearby location for weather prediction are utilised. The uncertainty introduced by using non-local measurements is approximately 1% above the PBL if the sonde was launched within 100 km and 6 hours of the lidar observation, assuming no frontal movements in that time [Russell et al., 1979]. Errors within the PBL will be greater and need to be assessed.

At ten sites across the UK, the UK Meteorological Office manages regular radiosonde measurements. These consist of two or three almost daily launches, reporting pressure, air and dew point temperature, altitude, wind speed and direction at synoptic pressure levels and other levels deemed necessary to characterise the atmosphere, though only pressure is reported at each level. The number density is derived assuming an ideal gas with pressure p and temperature T ,

$$N = \frac{p}{Tk_B}, \quad (3.14)$$

where k_B is Boltmann's constant. Nitrogen is assumed well mixed with number mixing ratio 0.78084 [NOAA, 1976].

To translate this data onto the vertical grid of the lidar, the altitude measurements available are linearly interpolated onto the logarithm of the pressure to estimate the altitude of each pressure level. The temperatures are then linearly interpolated onto the lidar's grid, an example of which is shown in figure 6. Each point is further linearly interpolated in time to the next radiosonde measurement to give a smoothly varying field for each lidar profile.⁵ Where there

⁵This neglects to note the time elapsed before the next sonde launch.

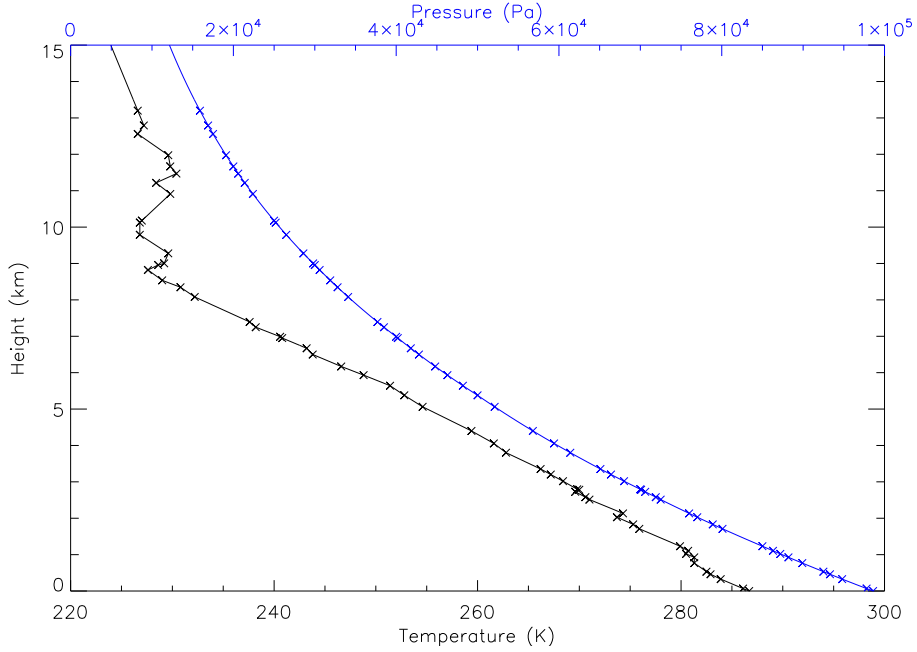


Figure 6: Example of interpolating radiosonde measurements, plotted as crosses, onto a lidar's vertical axis, plotted as a line. Sonde launched at Larkhill, Wiltshire on 2 Jul 2007 at 0549.

is a gap in the radiosonde data, a standard atmosphere [NOAA, 1976] is used, calibrated to surface observations.⁶

These fields are then used to estimate the transmission of the atmosphere due to molecular scattering. For a vertical beam ($R = z$),

$$\begin{aligned} \mathcal{T}_m(\lambda, z) &= \exp \left[- \int_0^z \alpha_m(\lambda, z') dz' \right] \\ &= \exp \left[- \int_0^z \sigma_R(\lambda) N(z') dz' \right], \end{aligned} \quad (3.15)$$

where σ_R is the Rayleigh scattering cross-section. This is calculated from the empirical fit derived in Bucholtz [1995],

$$\sigma_R(\lambda) = A\lambda^{-(B+C\lambda+D/\lambda)}, \quad (3.16)$$

where the constants are given in table 1. This demonstrates a fit of better than 0.2% to detailed calculations in the wavelength region this report considers.

For a gas with molar mass M and density ρ ,

$$\int_0^z \sigma_R(\lambda) N(z') dz' = \sigma_R(\lambda) \int_0^z \frac{N_A}{M} \rho(z') dz', \quad (3.17)$$

$$= \frac{\sigma_R(\lambda) N_A}{M} \int_{p(0)}^{p(z)} -\frac{dp'}{g}, \quad (3.18)$$

⁶The errors related to this have not yet been considered.

$\lambda_0(\mu\text{m})$	A	B	C	D
0.2 – 0.5	3.01577×10^{-28}	3.552142	1.35579	0.11563
> 0.5	4.01061×10^{-28}	3.99668	1.10298×10^{-3}	2.71393×10^{-2}

Table 1: The parameters of equation (3.16) for the empirical fit of the Rayleigh scattering cross-section from Bucholtz [1995].

$$= \frac{\sigma_R(\lambda)N_A}{Mg} [p(0) - p(z)], \quad (3.19)$$

where N_A is Avagadro's constant; g is the gravitational acceleration; and hydrostatic balance has been assumed in (3.18).

The Rayleigh backscatter coefficient is given by King [1923] as,

$$\beta_m(\lambda, z) = \frac{8\pi}{3}\sigma_R(\lambda)N(z). \quad (3.20)$$

3.3.2 Overlap function and constants

Whilst the meteorology changes continuously over time, the properties of the lidar system itself should remain constant until the system is adjusted by an operator. In the forward model, these are summarised by the calibration coefficients $C_{\text{el,ra}}$ and the overlap function $A(R, \varepsilon)$. In an ideal lidar system, these would be measured directly using spectroscopic equipment and ray tracing techniques. However, for a system with manual adjustment, it is impractical to determine the exact alignment of the laser and telescope for these calculations. Instead, these parameters can be estimated by calibration against a sky clear of aerosols, where the extinction and backscatter are known from Rayleigh scattering and the lidar equation can be solved for $A(R)$ [Wandinger and Ansmann, 2002]. Further, at most wavelengths, there is a significant error in the measurement of the Raman cross-section. This will dominate the uncertainty on C_{ra} , such that an absolute calibration of the system does not give a significant improvement [Sherlock et al., 1999; Leblanc and McDermid, 2008].

However, the atmosphere is never completely clear of aerosols, especially near the surface. Therefore, any knowledge of the aerosol distribution can improve the estimation of the overlap function from measurements. It has been observed that stable PBLs have similarly structured extinction profiles [He et al., 2008; Wiegner et al., 2006; Maurya et al., 2010]. Here, this is approximated as a constant value up to some height (not necessarily the top of the PBL), z_0 , and a rapid exponential decay above that over scale height H ,

$$\alpha_a(\lambda, z) = \begin{cases} \alpha_0, & z \leq z_0; \\ \alpha_0 \exp\left[\frac{z_0-z}{H}\right], & z > z_0. \end{cases} \quad (3.21)$$

The most readily obtained constraint on this profile is a measurement of its aerosol optical thickness (AOT) with a sun photometer. If the atmosphere has a total AOT of χ_∞ , the optical depth profile can be approximated by,

$$\chi_a(z) = \begin{cases} \frac{\chi_\infty z}{H+z_0}, & z < z_0; \\ \frac{\chi_\infty}{H+z_0} \left[z_0 + H \left(1 - \exp\frac{z_0-z}{H}\right)\right], & z \geq z_0. \end{cases} \quad (3.22)$$

Using this aerosol profile, the Raman profile (3.5) can be inverted to give what will be called the calibration curve,

$$C_{\text{ra}} A(R_i) \exp[-\chi_a(z)] = \frac{[n_{\text{ra}}(R_i) - n_B(\lambda_x)] R_i^2}{N_x(R_i)} \times \exp \left[\int_0^{R_i} \alpha_m(\lambda_L, r) + \alpha_m(\lambda_x, r) dr \right], \quad (3.23)$$

where $n_{\text{ra}}(R_i)$ and n_B have been corrected for PMT nonlinearity.

This inversion is well-suited to optimal estimation, taking a Raman profile and the AOT as its measurement vector, using equations (3.7) and (3.23) as its forward model, and having seven elements to its state vector — the four parameters of the overlap function (Δ , δ , ϕ_{\parallel} , and ϕ_{\perp}), z_0 , H , and the calibration constant of the Raman channel, C_{ra} . The derivatives of the forward model equations with respect to z_0 , H , and C_{ra} are elementary and those with respect to the overlap function parameters are summarised in Appendix E.4.

In the absence of weather, the PBL is most stable at night [Oke, 1987]. In addition to permitting an estimate of the extinction profile, a stable PBL permits the averaging of a lidar profile over several hours, giving excellent SNR into the stratosphere. Further, the lack of solar background gives substantially greater SNR for a lidar profile of the same duration than during the day. As such, though sun photometer measurements are not possible at night, this calibration scheme is best applied to night observations. If a star photometer is not available, the AOT can be estimated from the average of measurements at dusk and dawn.⁷

The selection of the most suitable data from that available is currently a qualitative choice. The period selected should be at least one hour from sunset to allow the mixing layer to collapse and be free of obvious clouds, haze, or other weather. The PBL height should remain constant during the period (± 50 m), which can be assessed using the observed attenuated backscatter coefficient, (2.19), as the height at which the ABC decreases significantly. If available, Doppler lidar wind measurements can also be used to assess the PBL winds. Average winds should be consistent with zero.

The *a priori* state defines an almost perfectly aligned system ($\Delta = \delta = \phi_{\parallel,\perp} = 10^{-6}$) as the derivatives at perfect alignment are exactly zero and the algorithm will not deviate from that state. The height and scale height of the aerosol layer are estimated to be of order 100 m and the order of magnitude of the calibration constant can be estimated from manufacturer's specifications of the efficiency of the PMT, interference filters, and other optics and the Raman cross-section.

The variances are determined from dimensional considerations. For example, in a coaxial system where the laser beam is reflected off the telescope's secondary mirror, δ is no greater than the size of the secondary mirror and, thus, the variance is estimated as order $(10 \text{ cm})^2$. The variance of the height and scale height of the aerosol layer are both taken as $(100 \text{ m})^2$ as the scale of stable boundary layers [Oke, 1987, chapter 2].

It then remains to determine the calibration constant of the elastic channel,

⁷The errors related to this have not been assessed.

assuming the overlap function is the same for each channel.⁸ Small variations in the backscatter coefficient have a substantially greater effect on the elastic profile than equivalent variations in the extinction have on the Raman profile. As such, only data above the tropopause is considered, where aerosol scattering will be negligible compared to molecular scattering (in the absence of recent, significant volcanic activity). The tropopause is defined as where the lapse rate tends to zero and is found by fitting against a temperature profile with lapse rate -6.5 K km^{-1} through the tropopause [NOAA, 1976].

Here, equation (3.4) can be solved for the elastic calibration constant,

$$C_{\text{el}} = \frac{[n_{\text{el}}(R_i) - n_B(\lambda_L)]R_i^2}{A(R_i, \varepsilon)\beta_m(R_i)} \exp \left[2 \int_0^{R_i} \alpha_m(r) \, dr \right] \quad (3.24)$$

This is then estimated by taking the mean of points above the tropopause with an SNR greater than unity.

3.3.3 Other parameters

A measure of the power emitted by the laser, E_L , can be obtained by directing a small fraction of the output beam to a calibrated power meter. For systems without this capability, a proxy for laser power was developed. It is the mean return in the first six bins of the elastic profile. This is successful in visually smoothing the data and will be compared to actual power measurements on such a system once a power meter can be installed.

The detector dark count can be estimated by averaging measurements when there should be no laser-induced radiance. Preferably, this would be measured just before the laser is fired, but for the systems used in this work, such measurements are not available. The last 300 bins of each measurement are used instead. For systems which report measurements beyond 30 km, this is an accurate estimate for all practical timescales, as the laser-induced radiance is negligible compared to the dark count. However, not all systems report to such heights, for which this method will overestimate the dark count. This is not yet accounted for in the retrieval.

The dead time of photon-counting PMTs can be determined using the methods described in Whiteman [2003]. Two profiles are acquired in quick succession — once with a neutral density filter attenuating the return and once without. The non-paralysable correction (3.10) is then applied to both profiles. The dead time is estimated as the value for which the ratio between the two signals is most constant with range. For detectors with an analogue mode, the comparison can be made against the analogue signal instead.

3.4 Summary

This retrieval scheme determines the maximum *a posteriori* solution of the equation,

$$\begin{pmatrix} \mathbf{n}_{\text{el}}^F \\ \mathbf{n}_{\text{ra}}^F \end{pmatrix} = \mathbf{F} \left[\begin{pmatrix} \boldsymbol{\beta}_a \\ \boldsymbol{\alpha}_a \end{pmatrix}, \mathbf{b} \right] + \boldsymbol{\epsilon}$$

⁸This implies that the light collected by the telescope is either well collimated in the optical system or the beam in that system is sufficiently small compared to the optics involved.

where the forward model, F , is summarised by the equations,

$$\begin{aligned}
n_j^F(R_i) &= \frac{n_j(R_i)}{1 + \frac{n_j(R_i)}{n_0} \frac{\tau_j}{\tau_d}}, \\
n_{\text{el}}(R_i) &= v_{\text{el}}(R_i) [\beta_m(R_i) + \beta_a(R_i)] \exp \left[-2 \int_0^{R_i} \alpha_a(r) \, dr \right] \\
&\quad + n_B(\lambda_L), \\
n_{\text{ra}}(R_i) &= v_{\text{ra}}(R_i) \exp \left[- \left(1 + \frac{\lambda_L}{\lambda_{N_2}} \right) \int_0^{R_i} \alpha_a(r) \, dr \right] \\
&\quad + n_B(\lambda_{N_2}), \\
v_{\text{el}}(R_i) &= \frac{C_{\text{el}} A(R_i, \varepsilon)}{R^2} \exp \left[-2 \int_0^{R_i} \alpha_m(r) \, dr \right], \\
v_{\text{ra}}(R_i) &= \frac{C_{\text{ra}} N_x(R_i) A(R_i, \varepsilon)}{R^2} \exp \left[- \left(1 + \frac{\lambda_L}{\lambda_{N_2}} \right) \int_0^{R_i} \alpha_m(r) \, dr \right].
\end{aligned}$$

4 First applications of the retrieval

4.1 Instruments

4.1.1 RACHEL

Transmitter	Receiver
Wavelength, 354.7 nm	Primary mirror diameter, 203 mm
Average pulse energy, ~ 45 mJ	Secondary mirror diameter, 75 mm
Repetition rate, 20 Hz	Focal length, 2 m
Beam diameter, 35 mm	Field of view, 0.2 mrad
Beam divergence, < 0.3 mrad	Bin length, 9 m
	Maximum range reported, 36.9 km

Table 2: Summary of the parameters of the RACHEL system, deduced from direct measurements and the manufacturer's specifications. The bin length can be altered by the operator, but this not been utilised.

The Robust and Compact Hybrid Environmental Lidar (RACHEL), developed by Hovemere Ltd., is the first of two Raman lidar systems used in this work. RACHEL is a four-channel, coaxial system designed to be cost-effective and easily transported for unattended operation as and when required in the field. It was designed after the introduction of the Kyoto Protocol to monitor carbon dioxide emissions from factories to enable monitoring and enforcement of the carbon trading scheme. Though this eventually proved infeasible due to the minuscule CO₂ signal, the scanning system developed for following industrial plumes provides the rare capacity of a lidar that can automatically scan the entire hemisphere of the sky. This enables monitoring of aerosol and cloud variations over the region around the lidar system rather than the more typical

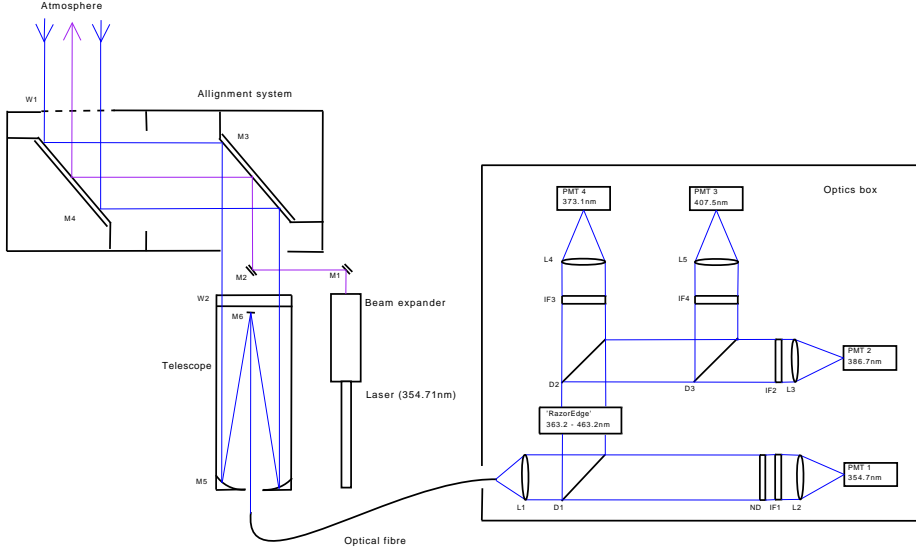


Figure 7: Schematic of the optical components of the RACHEL system, showing the scanning system, telescope, and optical system.

single zenith view. Further, with sufficient software, it should be possible to track a feature as it moves past the instrument.

To keep costs low, its utilises many ‘off-the-shelf’ components. The laser is a fairly common Continuum Nd:YAG model, frequency-tripled to 355 nm, observed by a commercially-available Meade Schmidt-Cassegrain telescope. The optical system, summarised in figure 7, uses dichroics to split the beam into four channels, which are further screened by interference filters. Though these are purpose-built components, they can be easily replaced to allow the monitoring of any species with sufficient concentration to be observable. Currently, the system is configured to observe, in addition to the elastic return, the Raman scattering from nitrogen (386.7 nm), water vapour (407.5 nm), and carbon dioxide (373.1 nm).

Measurements are made with photon-counting Hamamatsu PMT modules. Though ideal for the Raman signal, the elastic signal is sufficiently large for the first few kilometres to saturate this detector. Currently, this signal is attenuated with a neutral density filter in the elastic channel. In future, it is hoped to better utilise the available signal by using a beam splitter to instead direct the majority of the signal to a different PMT with lower gain. Though an internal power meter is installed within the laser cavity, it has not yet been possible to log these measurements. As such, the laser power proxy outlined in Section 3.3.3 is used with this data. This is necessary as, during 2010, the laser showed signs of damage and exhibited irregular and significant power fluctuations.

4.1.2 Chilbolton UV lidar

The other system used in this research is the Chilbolton UV Raman lidar (CUV). Designed and built by a team at the Rutherford Appleton Laboratory to monitor water vapour mixing ratio during the day, it is now permanently stationed

Transmitter	Receiver
Wavelength, 354.7 nm	Primary mirror diameter, 460 mm
Average pulse energy, 200 mJ	Secondary mirror diameter, 100 mm
Repetition rate, 50 Hz	Focal length, 2.0 m
Beam diameter, 10 mm	Field of view, 0.5 mrad
Beam divergence, 1.0 mrad	Bin length, 7.5 m
	Maximum range reported, 13.5 km

Table 3: Summary of the parameters of the CUV system, as reported by J. Agnew.

at the STFC Chilbolton Observatory at a rural site in Hampshire, England [Agnew, 2003]. The CUV monitors the elastic backscatter, the Raman scattering from nitrogen and water vapour, and the rotational anti-Stokes scattering from nitrogen (353.0 nm) and oxygen (353.9 nm) with two PMTs on each channel — one in the high-count rate analogue mode for observations in the PBL and the other in the photon-counting mode.

The system has been operated on a case study basis since 2002, reporting profiles of the attenuated backscatter coefficient (20 s, 7.5 m for 0.2 – 13 km) and water vapour mixing ratio (5 min, 22.5 m for 0.2 – 6 km) derived from the analogue measurements. As the instrument must be attended during operation, data is mostly from 10 AM to 4 PM on weekdays, though some exceptions exist.

For this work, access was kindly provided to the raw data for 30 clear or partly cloudy days from 2006 to 2010 [Agnew and Wrench, 2010]. As of yet, only the photon counting measurements have been used, though it is intended to consider both channels eventually. The relatively low maximum range reported has caused problems in the estimation of the dark count, but this is not believed to have caused significant difficulties in the retrievals.

4.2 Simulated data

The most controlled manner in which to investigate the performance of a retrieval scheme is through the use of simulated data. This is easily generated in an optimal estimation framework as the forward model determines the measurement that should be made from a given input state of the atmosphere. However, in the simulation of data, any processes that were neglected or simplified for the model used in retrievals should be reintroduced where possible. Though this will still omit any processes or inconsistencies that have not been considered at all, a retrieval scheme must be able to reliably retrieve data generated by its own forward model.

The significant effects to have been neglected in this work are multiple scattering and the exact nonlinearity of the detectors. In these simulations, these remain neglected as a full description of these effects has not yet been prepared.

4.2.1 Aerosol profile

Some thought must be given to the form of the atmospheric states that are input into the simulations. For a Levenberg-Marquadt retrieval scheme, it is

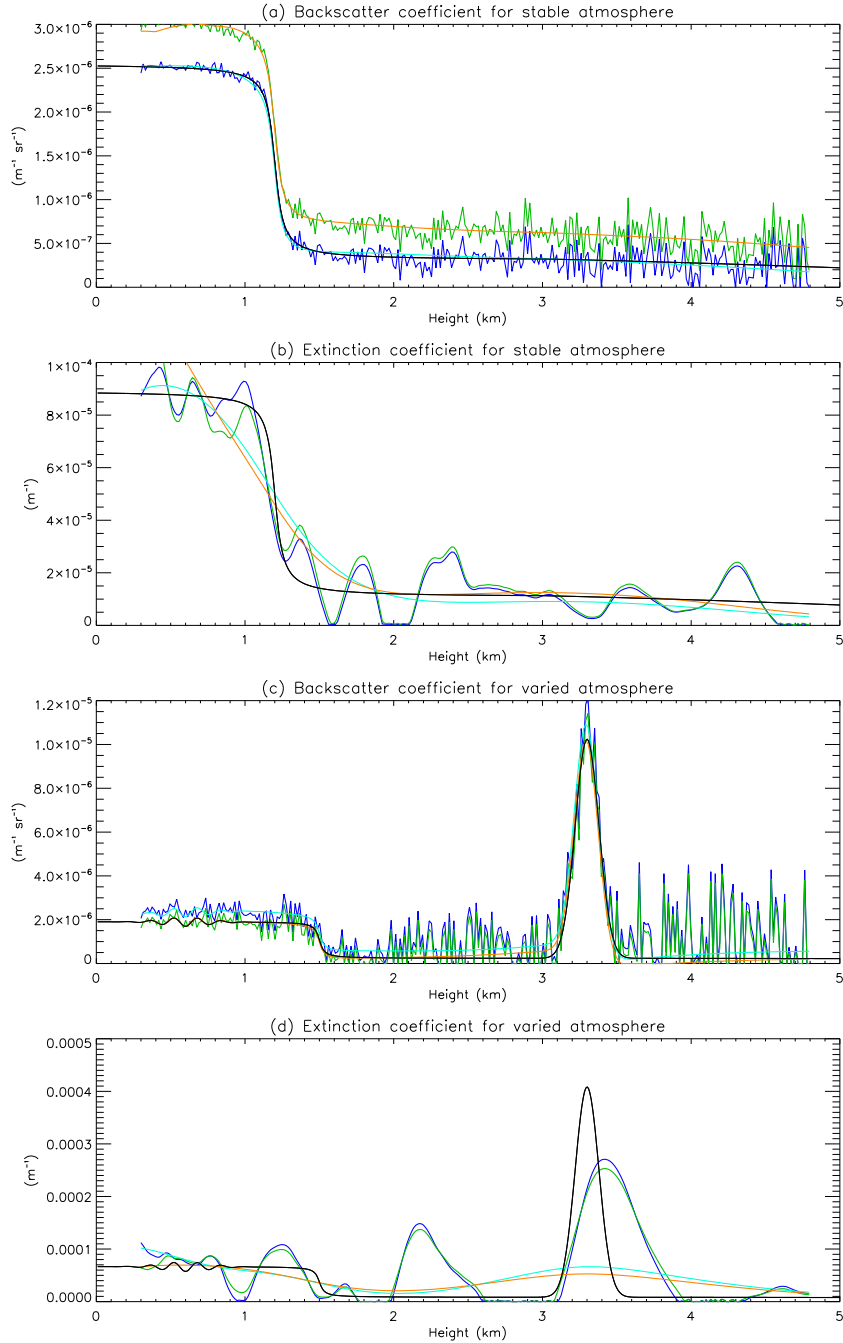


Figure 8: Retrievals from data simulated for the RACHEL system (table 2). The aerosol profiles, plotted in black, are modelled by equations (4.1) and (4.3) using the parameters summarised in table 4. Dark Blue — retrieval with parameter values used to generate the data with noise; Light blue — same but without noise; Green — retrieval with parameter values from calibration method with noise; Orange — same but without noise.

Plots	a (10^{-4} m $^{-1}$)	b (10^{-4} m $^{-1}$)	c	d (km)
(a) & (b)	0.50	0.25	8.67	1.2
(c) & (d)	0.38	0.19	9.27	1.5
Plots	R_0 (km)	R_1 (km)	B (sr $^{-1}$)	
(a) & (b)	3.0	10.0	35	
(c) & (d)	4.0	15.0	35	

Table 4: Parameters of (4.1) used in the generation of the simulated data for figure 8.

preferable for the profile to be continuous in its first derivative such that the scheme is more likely to converge to sensible solutions quickly.

As discussed in Section 3.3.2, the aerosol profile can be approximated as constant to some height, followed by a sharp, exponential decay. This is constructed as a function continuous in the first derivative with,

$$\alpha_a(\lambda, R) = \begin{cases} a - b \tan^{-1}[c(R - d)], & R < R_0; \\ e + fR + gR^2 + hR^3, & R_0 \leq R \leq R_1; \\ 0, & R > R_1, \end{cases} \quad (4.1)$$

where a, b, c, d control the shape of the profile and e, f, g, h solve,

$$\begin{pmatrix} 1 & R_1 & R_1^2 & R_1^3 \\ 1 & R_0 & R_0^2 & R_0^3 \\ 0 & 1 & 2R_1 & 3R_1^2 \\ 0 & 1 & 2R_0 & 3R_0^2 \end{pmatrix} \begin{pmatrix} e \\ f \\ g \\ h \end{pmatrix} = \begin{pmatrix} 0 \\ a - b \tan^{-1}[c(R_0 - d)] \\ 0 \\ -\frac{bc}{1+c^2(R_0-d)^2} \end{pmatrix}. \quad (4.2)$$

The boundaries $R_{0,1}$ are chosen arbitrarily.

The backscatter profile is determined by assuming a constant lidar ratio,

$$\beta(\lambda, R) = \frac{\alpha(\lambda, R)}{B}. \quad (4.3)$$

Two examples of such profiles are plotted in black in figure 8, using the parameter values given in table 4.

Features can be easily added to this profile, provided they tend to zero away from their centre. For example, it has been found in studies of algorithms to automatically detect clouds in ceilometer data that the backscatter profile of a cloud is well-modelled by a Gaussian (or a sum of Gaussians) [Biavati, 2011].

For plots 8c and 8d, to investigate the resolution limits of the algorithm, an oscillatory structure is added within the PBL of the form,

$$A \exp \left[-\frac{1}{2} \left(\frac{R - 0.6}{0.16} \right)^2 \right] \sin \frac{R}{0.08\pi}, \quad (4.4)$$

where $A = 2 \times 10^{-7}$ for backscatter; $A = 9 \times 10^{-6}$ for extinction; and R is in kilometers. A cloud is modelled by the Gaussian,

$$B \exp \left[-\frac{1}{2} \left(\frac{R - 3.3}{0.08} \right)^2 \right], \quad (4.5)$$

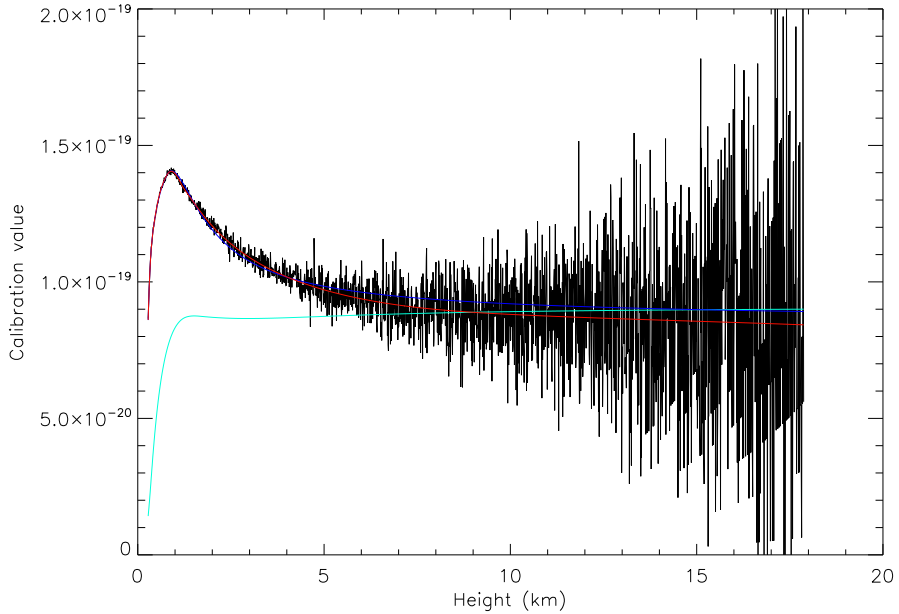


Figure 9: Application of the calibration scheme of section 3.3.2. Data simulated on the RACHEL system (table 2) using the parameters outlined in table 5. Black — calibration curve from simulated data with noise; Red — same but without noise; Light blue — first guess of an almost aligned system; Dark blue — result of the fitting (retrieved parameters listed in table 5).

where $B = 10^{-5}$ for backscatter and $B = 4 \times 10^{-4}$ for extinction. The exact parameter values used have no theoretical basis and were selected as being within the ranges observed in plots presented in a variety of lidar studies referenced in this report.

4.2.2 Calibration scheme

The calibration scheme outlined in Section 3.3.2 is most readily explored through simulated data, as the parameters it determines are not easily measured independently. Figure 9 shows the results of a fitting to simulated data. The black curve shows the simulated calibration curve, with a noiseless version plotted in red. A first guess of a well-aligned system is plotted in light blue and the result of the retrieval in dark blue. Errors are under assessment and are not given.

Up to 4 km, the retrieved function closely corresponds with the true form. Above that, the retrieved curve underestimates the true value by up to 10%. It is likely that this underestimation is related to the large noise on measurements above 10 km. This impact of this region could be reduced by using a more stringent threshold on the SNR.

The parameters of the overlap function used to simulate the data and those retrieved are given in lines 4 and 5 of table 5. The retrieved value of Δ is consistent with the truth, but the other values are significantly different. This may demonstrate a significant degeneracy in these parameters to a given func-

Figure	Δ (m)	δ (m)	ϕ_{\parallel} (deg)	ϕ_{\perp} (deg)
4 (black)	0	0	0	0
4 (blue)	-4.0×10^{-3}	0	0	0
4 (green)	7.0×10^{-3}	0	9.0×10^{-3}	7.0×10^{-3}
8 & 9 (black)	7.2×10^{-3}	2.7×10^{-3}	1.0×10^{-3}	1.0×10^{-5}
9 (dark blue)	7.1×10^{-3}	4.2×10^{-6}	1.3×10^{-6}	1.6×10^{-3}

Table 5: Parameters of the overlap function used throughout this report.

tional form, which concurs with the assumption that the beam shape assumed is not important to the final result. The Raman calibration constant was set as 1.70×10^{-17} and was retrieved to be 1.76×10^{-17} and the elastic calibration constant, set to 4.10×10^{13} , was retrieved as 3.96×10^{13} . Neither is consistent within the errors reported, which is believed to be related to the poor fit to the calibration above 5 km as this is the region with the greatest information content pertaining to the calibration constants.

As will be shown, these errors do not affect the shape of the retrieved profile, merely its magnitude. As the eventual aim is to produce extinction and backscatter retrievals with rigorously derived errors, this is not currently acceptable, but it is hoped with corrections in the implementation of the overlap function and the use of more stringent SNR limits, the scheme will produce suitable results.

4.2.3 Retrievals

The retrieval has been applied to a variety of different model atmospheres, two of which are highlighted in figure 8. These pairs of extinction and backscatter plots show the simulated aerosol profile in black. A retrieval initialised with the parameters used to generate the data is plotted in light blue (dark blue with noise) and one initialised from the calibration scheme is plotted in orange (green with noise). Errors are not plotted as the forward model errors have not yet been fully integrated.⁹

An example of a simple, stable atmosphere with an AOT of 0.125 is shown in figs. 8a and 8b. A more complex atmosphere with AOT of 0.189, featuring a thin, Gaussian cloud at 3.3 km and a sinusoid added to the PBL to mimic aerosol layers, is presented in figs. 8c and 8d. These are used to simulate profiles from five minutes of observations at night by RACHEL. The parameters used for the simulation are summarised in tables 2, 4, and 5.

The retrieval initialised to the true parameter values produces a very good fit of the backscatter for each model atmosphere, with or without noise, capturing the top of the PBL and the cloud very clearly. The smaller sinusoidal variations are only just detectable above the noise, the limits of which should be investigated more thoroughly, but are well fit in the absence of noise. An almost identical backscatter profile is retrieved when initialised with the calibration scheme, but with a high bias. The retrieval is capturing the shape of the

⁹Current estimates compare favourably to existing schemes for the backscatter retrieval, of order 1%, but the error on the extinction is reported as significantly greater than 100%.

aerosol profile, but is incorrectly determining its magnitude due to a calibration error.

The extinction retrievals are less impressive. Without noise, the retrieval indicates the degree of smoothing applied to the data is too large, as the top of the PBL is spread over almost 2 km in fig. 8b and the cloud in fig. 8d is very poorly fit. However, with noise, the profiles are perturbed to such an extent that distinguishing features from noise is impossible. They do, on average, follow the truth and it appears to have fit the cloud, though at a slightly greater height, but this cannot be distinguished from coincidence. The fit to the boundary layer is visually better in fig. 8b than the noiseless case, but, in general, there does not currently appear to be enough sensitivity from the Raman channel.

Normally, such lack of sensitivity would be compensated by increasing the correlation length expected in the data, but this length is already known to be too great. As such, it may be necessary to retrieve extinction from Raman measurements averaged over longer periods than the backscatter. This would require separating the elastic and Raman signals in the existing code, but by using a sliding window average rather than strictly adding values together, sufficient signal can be found to improve the retrieval.

4.3 Field measurements

4.3.1 Chilbolton Observatory

The RACHEL system was given its first extensive field test at the Chilbolton Observatory (51.14° N, 1.44° W, 84 m) from February to April of 2010. This rural site hosts a wide variety of meteorological instruments, including a Doppler lidar, a commercial ceilometer and Raman lidar, several clear air and cloud radars, particle sensors, and surface meteorology observations [STFC, 2011]. It also hosts an AERONET solar radiometer [Woodhouse and Agnew, 2011] and is only 16 km from radiosonde launches at Larkhill [UK Met Office, 2011], making the observatory an ideal site to calibrate and validate RACHEL.

In particular, RACHEL can be directly compared to the CUV, which uses a more energetic beam, fired more rapidly, and observed with a larger telescope, which should provide an understanding of the limitations of the new system. An example from during the flight ban after the Eyjafjallajökull eruption in April 2010 is shown in figure 10. The superior SNR of the CUV is obvious, clearly resolving layering of the volcanic ash in and just above the PBL¹⁰ and high clouds throughout the day. With minor averaging, RACHEL satisfactorily resolves features within the PBL during the morning, but observes only the thickest cloud. It should be noted that at this time, the RACHEL system was overdue for regular maintenance and the laser was performing at significantly less than full power.

In the afternoon, it appears that RACHEL gives a different response to the CUV, with the aerosol more strongly concentrated near the surface. This is partially a result of the use of a logarithmic colour scale and partially due to the fact that the RACHEL overlap function peaks at ~ 500 m and then decreases to an asymptote as in the green plot of figure 4 whilst the CUV more closely resembles the black plot, only reaching its maximum value at 1.5 km. This

¹⁰The aerosol is identified as ash due to the large depolarisation ratio observed by a Leo-sphere EZ lidar operated at the site for the University of Reading.

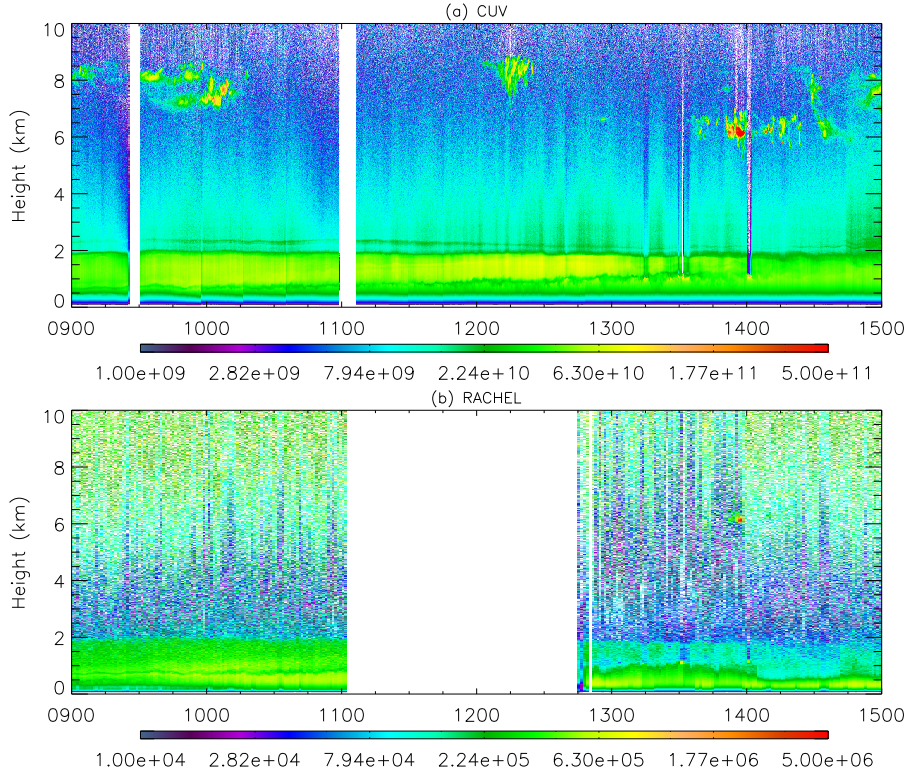


Figure 10: Uncalibrated ABC (2.19), not corrected for the overlap function, observed on 19 Apr 2010 during the Eyjafjallajökull eruption at the Chilbolton Observatory by (a) CUV at its raw resolution of 7.5 m and 20 s (1000 shots); and (b) RACHEL at raw 9 m resolution averaged over 1 min (1200 shots).

means the systems are most sensitive to PBL aerosols at different heights, giving visually different fields and demonstrating the importance of calibrating the systems to properly assess their results.

Despite the outstanding issues with the retrieval scheme developed in this work, it was applied to the available CUV data as an exploration of its response. An example of such a retrieval is shown in figure 11, compared to the results of the Klett algorithm outlined in Section 2.2 at the same resolution. Qualitatively, the optimal estimation scheme gives a superior result, both with and without cloud. As expected, the Klett scheme performs poorly in the presence of a cloud as this will reduce the SNR at the reference level. As the scheme integrates down from that level, deviations due to noise will be more significant and affect the quality of the result. In the clearer regions, the difficulties suffered by the Klett method would indicate that the reference level, here taken at 7 km, is not actually clear of aerosol. Either the profile should be averaged over a longer period, such that the reference height may be taken at a greater height which is more likely to be clear of aerosols or the scattering at the reference level should be estimated by an *ad hoc* method [Klett, 1985; Gross et al., 1995].

The optimal estimation scheme performed fairly well, as shown in the bottom two plots of figure 11. It mostly converged within a reasonable number

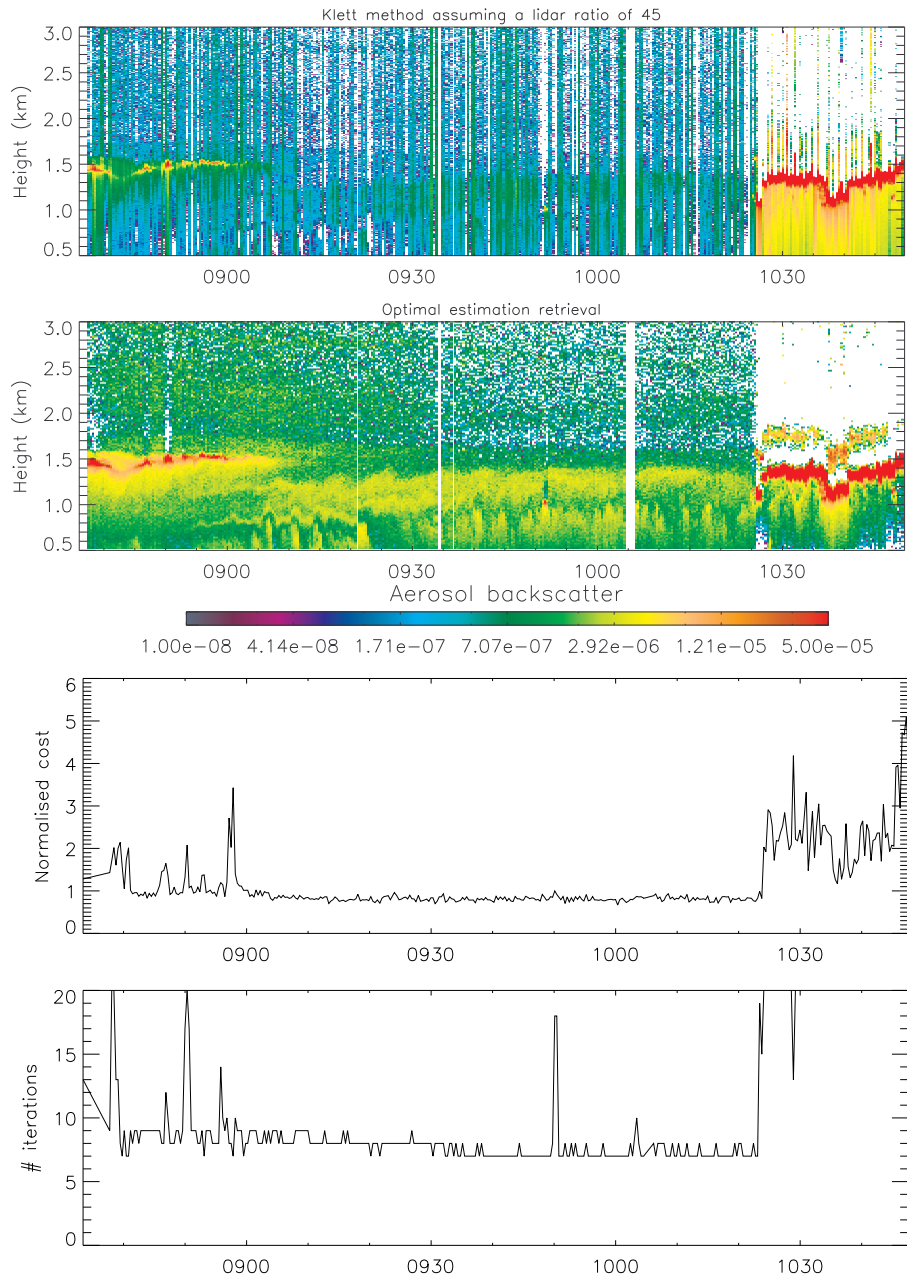


Figure 11: Aerosol backscatter on 29 Aug 2007 as derived by the Klett elastic algorithm (2.17), assuming a clear atmosphere at 7 km and a constant lidar ratio of 45 (top), and by optimal estimation retrieval, at a resolution of 20 s and 17 m (second down). For the optimal estimation scheme, the cost per measurement (third down) and number of iterations to convergence (bottom) are also shown.

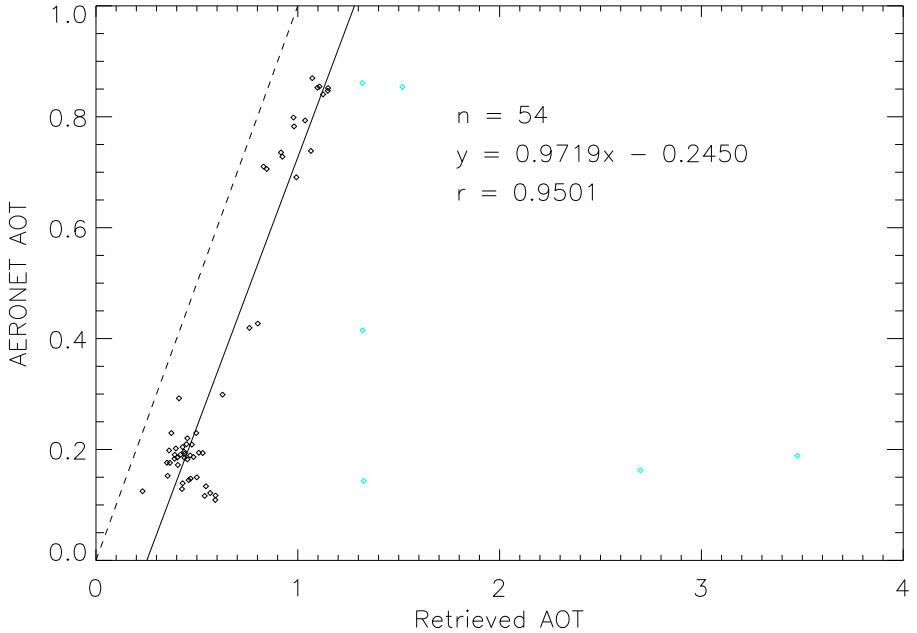


Figure 12: AOT at 355 nm retrieved by optimal estimation from CUV profiles against simultaneous, co-located AERONET measurements at 340 nm. The dotted line is the one-to-one line and the solid line, described by the parameters given on the plot, is the result of a least-squares regression of all black points. Blue points were found to have a cloud in the lidar's field of view and were neglected from the fit.

of iterations to a cost approximately equal to the length of the measurement vector. However, profiles containing thick cloud cover did not converge.¹¹ The strong backscatter of a cloud is a long way from the first guess of a clear sky and it may be that the application of a too stringent *a priori* variance constrains the retrieval to values smaller than are necessary. It is also possible that multiple scattering within the clouds makes the forward model no longer a good description of the system, causing the retrieval to fail. More investigation is required, but if a representation of multiple scattering is deemed necessary to model cloud observations, the methods outlined in Hogan [2008] should be appropriate, having been developed from the work of Eloranta [1998] for use in a joint lidar-radar optimal estimation scheme.

Intriguingly, despite the poor quality of the extinction profiles, it was found that there is merit in total AOT retrieved. Figure 12 was presented earlier this year [Povey et al., 2011], where 60 CUV profiles, averaged over one minute, which were taken coincident with an AERONET measurement at the same site were processed. The retrieved AOT was taken to be the total optical thickness retrieved at 10 km (the top of the profile). The AOT at 355 nm was estimated from AERONET measurements at 340 and 380 nm, assuming AOT is inversely proportional to wavelength. The plot shows the results of a linear least-square

¹¹The maximum number of iterations was 20.

regression between the two measures of AOT, where 6 profiles have been neglected from the fit (plotted in blue) as the lidar profile was found to contain a cloud. A correlation coefficient of 0.9501 was found, with a gradient of 0.9719, demonstrating a significant one-to-one relationship between the retrieved and measured quantities, though with a high bias. This plot was produced before the development of the calibration scheme and it is hoped that, with its completion, the bias will be corrected in future versions of this plot, serving as a validation of the retrieval scheme.

In all results presented, each retrieval starts from the same first guess — the *a priori* of a clear atmosphere. If, instead, the first guess is taken as the result of the previous retrieval, the number of iterations required for converge is significantly reduced. However, by running both forwards and backwards through the data, different results are obtained. This indicates that the retrieval is not properly converging and a more stringent threshold needs to be applied.

4.3.2 Central Oxford

In late July 2011, RACHEL was stationed on the roof of the Atmospheric Physics Building in central Oxford (51.43° N, 1.26° W, 70 m). Due to technical difficulties, data collection has not yet begun at this site, but it is hoped that regular observations of aerosol and cloud over Oxford can begin soon. A first sample of the data that RACHEL can provide is given in figure 13, showing the ABC at one minute resolution observed along the zenith. During the afternoon, a haze layer can clearly be seen and, through the night, cloud at all levels is observed, including the intrusion of a front from 3 AM and possible precipitation around 5 AM. The system is evidently much better prepared for regular observations than during its previous deployment, demonstrating greater stability of laser power.

5 Conclusions

Lidar is a powerful tool for atmospheric profiling, providing unprecedented temporal and spatial resolution within the troposphere. The response of a lidar is summarised by the lidar equation (2.14), describing the scattering properties of the atmosphere in terms of volume extinction and backscattering coefficients. To derive these independently requires measurements beyond just the elastic scattering of the laser beam. One possibility is the inelastic Raman backscattering of the beam by a well-mixed species in the atmosphere, as summarised by (2.21).

Retrieval schemes such as those described in Section 2 have proven successful in presenting qualitative observations of the evolution of clouds and aerosols and in observing turbulent motions, using aerosol as a tracer. However, these often rely on assumptions about the composition of the aerosol observed, require extensive smoothing, and cannot provide the rigorously-derived errors of satellite data products. Considering the small scales over which cloud-aerosol interactions occur, lidars are well placed to produce results that can complement satellite data to help understand these processes if data analysis techniques can be developed to allow better comparison between lidar and satellite data.

As such, an optimal estimation scheme for lidar is under development. This

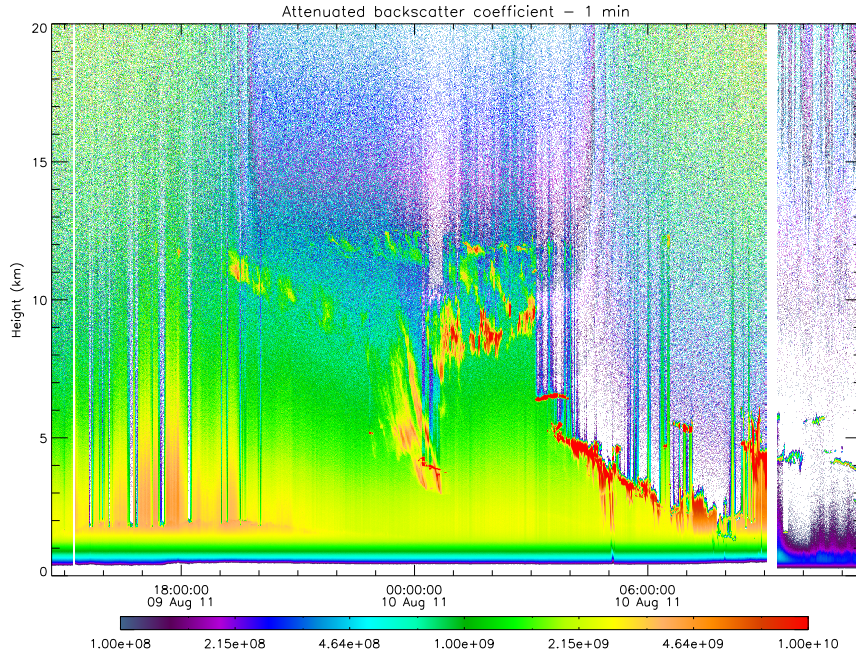


Figure 13: ABC observed over Oxford by RACHEL, averaged to 1 min. The dark region on the morning of the 10th of August is where a neutral density filter was installed in the channel to reduce detector saturation in the BL. Before this time, results below 1.5 km should be neglected due to saturation.

derives the aerosol extinction and backscatter from measurements of the elastic scattering and the Raman scattering of nitrogen. A calibration scheme has also been developed to estimate an instrument's response when it is impractical to measure in the laboratory. This uses a simple model of the aerosol extinction profile in a stable PBL to fit a parametrisation of the overlap function to observations of a clear night.

Neither scheme is yet complete. The calibration scheme has been shown to retrieve parameters that permit the primary scheme to accurately retrieve the shape of the aerosol backscatter profile, but with significant bias in its magnitude. There is also currently insufficient information available for the retrieval of the extinction profile, though the aerosol optical thickness derived from this profile was found to be highly correlated with coincident measurements by a solar radiometer, indicating the retrieval scheme is qualitatively working. It is hoped that with alterations to the formulation of the overlap function and further debugging, the calibration scheme will converge to sufficient accuracy to permit the primary retrieval scheme to work accurately. If it doesn't, the calibration scheme should be abandoned and the methods of Wandinger and Ansmann [2002] used instead, though this will require an assessment of the error involved in that method.

The sensitivity of the algorithms to their initial conditions needs to be properly assessed and, if found to be significant, the values used need to be justified. Further, the convergence criterion need to be reviewed. However, all of this

Year three	Planned tasks
First quarter	Initial data collection in Oxford with RACHEL and outline of measurement strategy; Installation of weather station; Validation of retrieval scheme against Chilbolton data; Submission of paper summarising scheme to peer-reviewed journal
Second quarter	Semi-continuous observation of Oxford and confirmation of measurement strategy; Streamlining of retrieval code for more efficient computation; Analysis of data collected at Chilbolton, including the Eyjafjallajökull eruption
Third quarter	Final observations in Oxford with RACHEL; Possible transfer of RACHEL to new site; Analysis of Oxford data; Transfer of knowledge of retrieval algorithm to Hovemere Ltd. for usage in commercial applications; Thesis writing
Fourth quarter	Thesis writing; Advising Hovemere

Table 6: Plan of work for year three.

work should be completed this year and both schemes should be submitted for peer-reviewed publication by Christmas. This would ensure that feedback from the review process is available before the main work of thesis writing begins.

That thesis is expected to contain eight chapters:

1. Introduction — an overview of the concepts covered in the thesis, including a summary of the use of lidars in the study of the atmosphere, the importance of aerosol to the global energy budget and a review of current methods of measuring its concentration, and the physics of Raman lidar.
2. The analysis of lidar data — this will derive from section 2 of this report, summarising the existing methods of interpreting lidar data. Primarily concentrating on the Klett and Ansmann algorithms, it will review the known applications and limitations of these methods and discuss how lidar data is used in conjunction with other data sources, particularly with regard to aerosol studies.
3. Techniques of Raman lidar — this chapter will outline the technical details of the lidar systems utilised later in the report, currently the Chilbolton UV lidar and RACHEL. Schematics of the apparatus and a summary of the control software and standard practices will be provided.
4. Calibration of a lidar system — a substantial expansion of section 3.3.2, describing the scheme to determine the overlap function and calibration constants of a lidar system by fitting an analytic form of the overlap function and simple model of the extinction profile to measurements of a clear night with stable PBL. There will also be an assessment of the accuracy of the scheme compared to existing methods and its application to simulated and real data.
5. Backscatter and extinction retrieval by optimal estimation — similar to section 3 of this report, detailing the optimal estimation retrieval scheme

and evaluating its performance against simulated data.

6. Application of the retrieval — the validation of the retrieval scheme. Figure 12 will be re-evaluated, comparing AOT retrieved from CUV data over several years to coincident AERONET measurements. Similar comparisons will be performed between retrievals from RACHEL in Oxford and a portable sun photometer (if a photometer can be obtained). Retrieved profiles will be compared with the results of the algorithms discussed in chapter 2, evaluating the capabilities of the new scheme and its consistency with existing knowledge.
7. Case studies — this chapter would apply the retrieval algorithm to address some matters of scientific interest. The content of this chapter is highly dependant on the success of the data collection campaign with RACHEL in Oxford, but at the very least would consider two existing data sets. Firstly, the available CUV data would be processed with an aim to identify any correlations between the scattering properties of aerosols and distance from a cloud. If found, such correlations could potentially demonstrate interactions between clouds and aerosols on scales not usually resolved. Secondly, observations of the Eyjafjallajökull eruption of April 2010 were made with several lidars. These will be processed with the aims of (a) estimating the mean ash concentration for comparison against other estimates from a variety of platforms and (b) investigating the changes in the aerosol over several days, such as an increase in the lidar ratio which would indicate a settling of larger particles (which have smaller lidar ratios).
8. Conclusions — a summary of the thesis and assessment of the value of the retrieval scheme to measurement of aerosols.

The RACHEL system will be deployed in central Oxford until at least April and preferably for a year. It is important to begin regular measurements as soon as possible by ensuring the necessary repairs and upgrades are completed during October. Then a measurement strategy should be developed dependant on the capabilities of the repaired system. Two particular investigations are currently considered and one should be selected and pursued.

In the worst acceptable case that the instrument only performs to the standards observed at Chilbolton in 2010, RACHEL would be used to investigate the horizontal homogeneity of aerosol in an urban environment. Retrievals of extinction and backscatter from a single channel can be performed, assuming horizontal homogeneity, by processing several profiles at different zenith angles [Althausen et al., 2000; Kovalev et al., 2007]. The validity of such methods can be investigated utilising RACHEL's scanning capacity to retrieve extinction and backscatter around Oxford and determine the length and time scales over which the aerosol can be considered homogeneous. It is hoped that it will be possible to resolve sources of aerosol, such as lorry traffic on the A34, in which case the length scales over which such forcing acts can be investigated.

Oxford is an interesting location as it is a relatively compact city surrounded in fields and rural terrain. If RACHEL is capable of resolving aerosols up to 10 km away, it should be possible to investigate the mixing of the more polluted urban air in the city centre with cleaner rural air beyond the ring road, which should provide insight into the impact of new settlements on surrounding air quality.

These case studies all aim to investigate the scales over which aerosol properties vary. Current satellite studies assume aerosol properties can be averaged over several hundred kilometers and periods of weeks. However, the processes by which aerosols are produced, such as combustion, occur over significantly smaller temporal and physical scales. Further, numerous published lidar papers detail small-scale variations in aerosol activity under a variety of conditions, such as urban pollution plumes. This raises the question if the scales at which aerosols are currently studied is the most suitable compared to the rate with which they disperse to larger scales. A scanning Raman lidar is the most suitable instrument to investigate these interactions due to its superior temporal and spatial resolution.

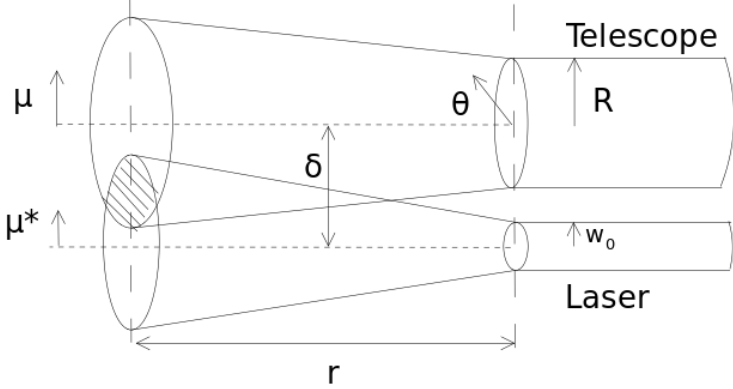


Figure 14: A schematic of the optical axes of a lidar system.

A Derivation of effective area

The overlap function defined in equation (2.8) will have a value of zero very close to the instrument, where there is no overlap between the laser beam and telescope's FOV and will ideally equal unity above some height where they overlap completely. As such, it is common in lidar work to neglect the overlap function by only considering measurements from beyond that range. For work in the free troposphere, this assumption is generally found to be valid [Velotta et al., 1998]. However, when considering the PBL and ranges less than 2 km, it is possible that the effective area will be varying in a significant way. A knowledge of the instrument's effective area is required to avoid underestimating the true backscatter in these regions. If the arrangement optical system is well known, this can be determined from ray tracing software. If not, geometrical optics can be used to determine an approximate functional form. This appendix derives such a function, summarised by equations (3.7) and (3.8).

A.1 Overlap of the laser beam and telescope FOV

This section outlines with the method of Halldórsson and Langerholc [1978], using the notation of Measures [1992, chapter 7.4].

Assume, at first, a simple model of the beam shape with constant intensity across a circular cross-section of radius $w(z)$,

$$\psi(z, \mathbf{r}) = H[w(z) - |\mathbf{r}|], \quad (\text{A.1})$$

where $|\mathbf{r}|$ is the radial distance from the centre of the vertical beam; and H is the Heaviside step function.

By defining a cylindrical coordinate system (μ, θ, z) about the axes of the telescope, as shown in figure 14,

$$|\mathbf{r}| = \sqrt{\mu^2 + d^2 - 2d\mu \cos \theta}, \quad (\text{A.2})$$

$$dA(z, \mathbf{r}) = \mu d\mu d\theta, \quad (\text{A.3})$$

where d is the perpendicular distance between the optical axis of the laser and telescope.

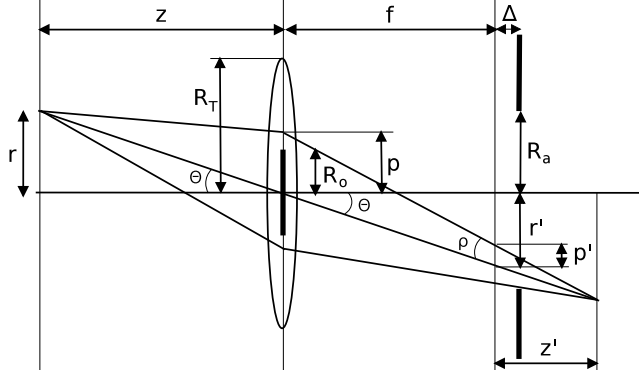


Figure 15: A Cassegrain telescope modelled by a lens, radius R_T and focal length f , with a central obstruction, radius R_o . An object at distance z from the lens plane and radial distance r from the optical axis is imaged through an aperture, radius R_a , in a plane a distance Δ beyond the focal plane. The image is focused a distance z' from the focal plane. It produces a spot of radius p on the lens and a spot of radius p' , centre a distance r' from the optical axis, in the image plane.

Substituting (A.1), (A.2), and (A.3) into (2.8),

$$\begin{aligned} A(z) &= \frac{A_0}{A_L(z)} \int \psi(z, \mathbf{r}) \xi(z, \mathbf{r}) dA(z, \mathbf{r}), \\ &= \frac{R_T^2}{w^2(z)} \int_0^\infty \int_0^{2\pi} H[w(z) - |\mathbf{r}|] \xi(z, \mu, \theta) \mu d\mu d\theta. \end{aligned} \quad (\text{A.4})$$

The flux that couples with the detector, ξ , is the fraction of the image spot that passes through the detector's aperture. The function $\mathcal{A}(r_1, r_2; \mu)$ is defined as the overlap area of two circles, radii r_1 and r_2 , with distance μ between their centres. Using this,

$$\xi(r, z) = \frac{\mathcal{A}(R_a, R'_T; \mu') - \mathcal{A}(R_a, R'_o; \mu')}{\pi R_T'^2}, \quad (\text{A.5})$$

where the second term represents the area obscured by the secondary mirror; $R'_{T,o}$ are the radii of image spots in the detector's plane produced by the entire lens and the obstruction, respectively; and μ' is the distance between their centres in that plane.

A Cassegrain telescope, focal length f , can be modelled by the lens system of figure 15. The radii of the lens, central obstruction, and exit aperture are taken as the radii of the telescope's primary and secondary mirrors and the detector's aperture, respectively.

Considering the central ray of the lens, the displacement of the centre of the image spot on the detector from the optical axis, r' , is found to be,

$$\tan \Theta = \frac{r}{z} = \frac{r'}{f + \Delta} \quad (\text{A.6})$$

$$r' = \frac{(f + \Delta)r}{z} \equiv \gamma \frac{fr}{z}, \quad (\text{A.7})$$

where $\gamma = 1 + \Delta/f$; Δ is the displacement of the detector from the focal plane; and the object is a distance z from the telescope's plane and radial distance r from its optical axis.

A similar expression for the radius of the image spot in the detector plane, p' , can be found in terms of the radius of the illuminated area on the lens, p , by considering similar triangles about the angle ρ ,

$$\frac{p'}{p} = \frac{|z' - \Delta| \cos \Theta}{(f + z') \cos \Theta} = \frac{|z' - \Delta|}{f + z'}. \quad (\text{A.8})$$

By the lens maker's formula,

$$\frac{1}{f} = \frac{1}{z} + \frac{1}{f + z'}, \quad (\text{A.9})$$

$$f + z' = \frac{fz}{z - f}, \quad (\text{A.10})$$

$$z' = \frac{f^2}{z - f}. \quad (\text{A.11})$$

Substituting this into (A.8),

$$p' = p \left| \frac{f^2}{z - f} - \Delta \right| \sqrt{\frac{fz}{z - f}}, \quad (\text{A.12})$$

$$= \frac{fp}{z} \left| 1 + \frac{\Delta}{f} - \frac{\Delta z}{f^2} \right|, \quad (\text{A.13})$$

$$= \nu(z) \frac{fp}{z}, \quad (\text{A.14})$$

where $\nu(z) = \left| \gamma - \frac{\Delta z}{f^2} \right|$. The z dependence will be dropped from this expression for brevity.

Using (A.7) and (A.14) in (A.5),

$$\xi(\mu, z) = \frac{\mathcal{A}\left(R_a, \frac{\nu f R_T}{z}; \frac{\gamma f \mu}{z}\right) - \mathcal{A}\left(R_a, \frac{\nu f R_o}{z}; \frac{\gamma f \mu}{z}\right)}{\pi (\nu f R_T/z)^2}. \quad (\text{A.15})$$

It is shown in Appendix A.3 that,

$$\mathcal{A}(r_1, r_2; \mu) = \begin{cases} 0, & \mu \geq r_1 + r_2; \\ \pi \min[r_1^2, r_2^2], & \mu \leq |r_1 - r_2|; \\ r_1^2 \cos^{-1}\left(\frac{\mu^2 + r_1^2 - r_2^2}{2\mu r_1}\right) + r_2^2 \cos^{-1}\left(\frac{\mu^2 + r_2^2 - r_1^2}{2\mu r_2}\right) \\ - \frac{1}{2}[(r_1 + r_2)^2 - \mu^2][\mu^2 - (r_1 - r_2)^2]^{1/2}, & \text{otherwise.} \end{cases} \quad (\text{A.16})$$

Using the fourth-order symmetry of this expression,

$$\mathcal{A}(r_1, cr_2; c\mu) \equiv c^2 \mathcal{A}(c^{-1}r_1, r_2; \mu). \quad (\text{A.17})$$

Hence, equation (A.15) can be rewritten as,

$$\xi(\mu, z) = \frac{1}{\pi} \left(\frac{\gamma}{\nu R_T} \right)^2 \left[\mathcal{A}\left(\frac{\nu z}{\gamma f} R_a, \frac{\nu}{\gamma} R_T; \mu\right) - \mathcal{A}\left(\frac{\nu z}{\gamma f} R_a, \frac{\nu}{\gamma} R_o; \mu\right) \right],$$

$$\equiv \frac{1}{\pi} \left(\frac{\gamma}{\nu R_T} \right)^2 [\mathcal{A}(\alpha, \rho_T; \mu) - \mathcal{A}(\alpha, \rho_o; \mu)], \quad (\text{A.18})$$

where $\alpha = \frac{\nu z}{\gamma f} R_a$ and $\rho_{T,o} = \frac{\nu}{\gamma} R_{T,o}$, again neglecting to denote the z dependence.

Substituting into (A.4),

$$A(z) = \frac{(\gamma/\nu)^2}{\pi w^2(z)} \int_0^\infty \int_0^{2\pi} H[w(z) - |\mathbf{r}|] \times [\mathcal{A}(\alpha, \rho_T; \mu) - \mathcal{A}(\alpha, \rho_o; \mu)] \mu d\mu d\theta. \quad (\text{A.19})$$

In this, $H[w(z) - |\mathbf{r}|]$ represents a circle of radius $w(z)$ centred at a radial distance $d(z)$ from the optical axis and $\mu d\mu d\theta$ represents a circle of radius μ about that axis. Hence, the function \mathcal{A} can be used to rewrite (A.19) as,

$$A(z) = \frac{(\gamma/\nu)^2}{\pi w^2(z)} \int_{\mu=0}^{w(z)+d(z)} [\mathcal{A}(\alpha, \rho_T; \mu) - \mathcal{A}(\alpha, \rho_o; \mu)] d\mathcal{A}[\mu, w(z); d(z)]. \quad (\text{A.20})$$

where, when there is a misalignment in the axes of the laser and telescope,

$$d(z) = \sqrt{(\delta + \phi_{\parallel} z)^2 + (\phi_{\perp} z)^2}, \quad (\text{A.21})$$

using $\phi_{\parallel, \perp}$ as the angles between the laser and telescope axes parallel and perpendicular to the plane defined by the telescope axis and the laser pupil.

The overlap function can then be expressed as,

$$A(z) = \left[\frac{\gamma}{\nu w(z)} \right]^2 [S_H(\rho_T, z) - S_H(\rho_o, z)], \quad (\text{A.22})$$

where the problem is now reduced to solving the integral,

$$S_H(\rho, z) = \frac{1}{\pi} \int_{\mu=0}^{w(z)+d(z)} \mathcal{A}(\alpha, \rho; \mu) d\mathcal{A}[\mu, w(z); d(z)]. \quad (\text{A.23})$$

When $w(z) + d(z) \leq |\alpha - \rho|$ the integrand is constant as the laser beam is completely within the telescope's FOV, giving case 2 of (3.8),

$$S_H(\rho, z) = \int_{\mu=0}^{w(z)+d(z)} \min[\alpha^2, \rho^2] d\mathcal{A}[\mu, w(z); d(z)], \quad (\text{A.24})$$

$$= \pi w^2(z) \min[\alpha^2, \rho^2]. \quad (\text{A.25})$$

Otherwise, integration by parts gives,

$$S_H(\rho, z) = \frac{1}{\pi} \left\{ \begin{aligned} & \{\mathcal{A}[\alpha, \rho; \mu] \mathcal{A}[\mu, w(z); d(z)]\}_0^{w(z)+d(z)} \\ & - \int_{\mu=0}^{w(z)+d(z)} \mathcal{A}[\mu, w(z); d(z)] d\mathcal{A}(\alpha, \rho; \mu) \end{aligned} \right\}. \quad (\text{A.26})$$

In Appendix A.4 it is shown that,

$$d\mathcal{A}(\alpha, \rho; \mu) = \begin{cases} -\sqrt{\Upsilon(\alpha, \rho; \mu)} \frac{d\mu}{\mu}, & |\alpha - \rho| \leq \mu \leq \alpha + \rho \\ 0, & \text{otherwise,} \end{cases} \quad (\text{A.27})$$

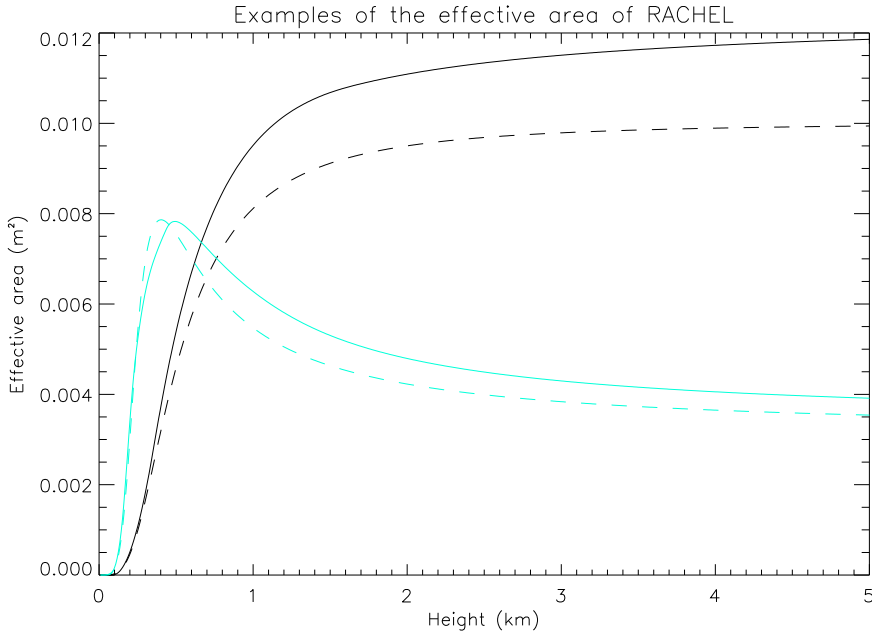


Figure 16: Examples of the Halldórsson and Langerholc [1978] model of effective area for the RACHEL system. The solid lines use a continuous beam profile and the dashed a Gaussian beam profile. Black — a perfectly aligned system; Blue — a misaligned system.

where $\Upsilon(\alpha, \rho; \mu) = [(\alpha + \rho)^2 - \mu^2][\mu^2 - (\alpha - \rho)^2]$.

Correcting the original paper of Halldórsson and Langerholc [1978], the limits of the integral (A.26) are altered such that $d\mathcal{A} \neq 0$. Hence, using (A.16) to evaluate $\mathcal{A}[w(z) + d(z), w(z), d(z)]$,

$$\begin{aligned} S_H(\rho, z) &= w^2(z)\mathcal{A}[\alpha, \rho; w(z) + d(z)] \\ &\quad + \frac{1}{\pi} \int_{|\alpha-\rho|}^{\Lambda} \mathcal{A}[\mu, w(z); d(z)] \sqrt{\Upsilon(\alpha, \rho; \mu)} \frac{d\mu}{\mu}, \end{aligned} \quad (\text{A.28})$$

where $\Lambda = \min[w(z) + d(z), \alpha + \rho]$. The first term is non-zero for $w + d < \alpha + \rho$, as in cases 7 – 9 of (3.8).

Thus, the overlap function can be determined by numerical integration of equation (A.28). A generic beam profile may be applied by replacing the $H[x]$ function of equation (A.19) and evaluating both the radial and angular integrals. Figure 16 shows examples of the overlap functions for the RACHEL system (see section 4.1.1) for continuous and Gaussian beam profiles, plotted as solid and dashed lines respectively, using the same system parameters.

In this work, a flat beam profile is used as it is significantly faster. Though a flat profile will be a poor model for the beam, this form will be fit to measurements rather than be determined from known parameters. As such, the parameters derived will not be physically meaningful, but the curve produced should be a good estimate of the truth.

A.2 Further evaluation

The integral of equation (A.28) can be cumbersome to evaluate numerically and often does not converge under a Romberg integration. The efficiency of this calculation can be significantly improved by moving beyond the work of Halldórsson and Langerholc [1978] to evaluate this term in various limits. z dependences will be neglected throughout this section. Firstly, define,

$$\kappa_H(\rho, z) = \frac{1}{\pi} \int_{|\alpha-\rho|}^{\Lambda} \mathcal{A}[\mu, w; d] \sqrt{\Upsilon(\alpha, \rho; \mu)} \frac{d\mu}{\mu}. \quad (\text{A.29})$$

The integrand is zero where $\mu \leq d - w$. Hence, if $\alpha + \rho \leq d - w$, $\kappa_H = 0$, being case 1 of (3.8). In general, the lower limit is changed to,

$$\kappa_H(\rho, z) = \frac{1}{\pi} \int_{\Gamma}^{\Lambda} \mathcal{A}[\mu, w; d] \sqrt{\Upsilon(\alpha, \rho; \mu)} \frac{d\mu}{\mu}, \quad (\text{A.30})$$

where $\Gamma = \max[|\alpha - \rho|, d - w]$.

The integrand takes one of two forms, depending on if $\mu \leq w - d$. Hence,

$$\kappa_H(\rho, z) = \int_{\Gamma}^{w-d} \mu \sqrt{\Upsilon(\alpha, \rho; \mu)} d\mu + \int_{w-d}^{\Lambda} \mathbb{A}[\mu, w; d] \sqrt{\Upsilon(\alpha, \rho; \mu)} \frac{d\mu}{\mu}, \quad (\text{A.31})$$

where,

$$\begin{aligned} \mathbb{A}(\mu, w; d) = & \frac{1}{\pi} \left[\mu^2 \cos^{-1} \left(\frac{d^2 + \mu^2 - w^2}{2d\mu} \right) + w^2 \cos^{-1} \left(\frac{d^2 - \mu^2 + w^2}{2dw} \right) \right. \\ & \left. - \frac{\sqrt{\Upsilon(\mu, w; d)}}{2} \right]. \end{aligned}$$

The remaining cases of (3.8) then derive from considering this in various limits:

- $d - w < |\alpha - \rho| < \alpha + \rho < w - d < w + d$ — The second term of (A.30) doesn't exist and κ_H can be evaluated exactly to give case 3 of (3.8),

$$\kappa_H(\rho, z) = \int_{|\alpha-\rho|}^{\alpha+\rho} \mu \sqrt{\Upsilon(\alpha, \rho; \mu)} d\mu, \quad (\text{A.32})$$

$$\begin{aligned} &= \left[\frac{\mu^2 - \alpha^2 - \rho^2}{4} \sqrt{\Upsilon(\alpha, \rho; \mu)} \right. \\ &\quad \left. + 2\alpha^2 \rho^2 \tan^{-1} \sqrt{\frac{\mu^2 - (\alpha - \rho)^2}{(\alpha + \rho)^2 - \mu^2}} \right]_{|\alpha-\rho|}^{\alpha+\rho}, \quad (\text{A.33}) \end{aligned}$$

$$= \pi \alpha^2 \rho^2. \quad (\text{A.34})$$

- $|w - d| < |\alpha - \rho| < \Lambda$ — The first term of (A.30) doesn't exist to give cases 4 and 7 of (3.8). For $\alpha + \rho < w + d$, κ_H is then integrated by parts to avoid rounding errors for $\rho \ll 1$,

$$\kappa_H(\rho, z) = \int_{|\alpha-\rho|}^{\Lambda} \mathbb{A}[\mu, w; d] \sqrt{\Upsilon(\alpha, \rho; \mu)} \frac{d\mu}{\mu}, \quad (\text{A.35})$$

$$= [-\mathbb{A}(\mu, w; d)\pi\mathbb{A}(\alpha, \rho; \mu)]_{|\alpha-\rho|}^{\alpha+\rho} + \int_{|\alpha-\rho|}^{\alpha+\rho} 2\mu \cos^{-1} \left(\frac{d^2 + \mu^2 - w^2}{2d\mu} \right) \mathbb{A}(\alpha, \rho; \mu) d\mu, \quad (\text{A.36})$$

$$= \pi \min[\alpha^2, \rho^2] \mathbb{A}(|\alpha - \rho|, w; d) \quad (\text{A.37})$$

$$+ 2 \int_{|\alpha-\rho|}^{\alpha+\rho} \mu \cos^{-1} \left(\frac{d^2 + \mu^2 - w^2}{2d\mu} \right) \mathbb{A}(\alpha, \rho; \mu) d\mu. \quad (\text{A.38})$$

- $|\alpha - \rho| < d - w < \Lambda$ — The first term of (A.30) doesn't exist to give cases 5 and 8 of (3.8),

$$\kappa_H(\rho, z) = \int_{d-w}^{\Lambda} \mathbb{A}[\mu, w; d] \sqrt{\Upsilon(\alpha, \rho; \mu)} \frac{d\mu}{\mu}. \quad (\text{A.39})$$

- $d - w < |\alpha - \rho| < w - d < \Lambda$ — Both terms of (A.30) exist and the first can be evaluated exactly to give cases 6 and 9 of (3.8),

$$\begin{aligned} \kappa_H(\rho, z) &= \int_{|\alpha-\rho|}^{w-d} \mu \sqrt{\Upsilon(\alpha, \rho; \mu)} d\mu + \int_{w-d}^{\Lambda} \mathbb{A}[\mu, w; d] \sqrt{\Upsilon(\alpha, \rho; \mu)} \frac{d\mu}{\mu}, \\ &= \frac{(w-d)^2 - \alpha^2 - \rho^2}{4} \sqrt{\Upsilon(\alpha, \rho; w-d)} \\ &\quad + 2\alpha^2 \rho^2 \tan^{-1} \sqrt{\frac{(w-d)^2 - (\alpha-\rho)^2}{(\alpha+\rho)^2 - (w-d)^2}} \\ &\quad + \int_{w-d}^{\Lambda} \mathbb{A}[\mu, w; d] \sqrt{\Upsilon(\alpha, \rho; \mu)} \frac{d\mu}{\mu}. \end{aligned} \quad (\text{A.41})$$

A.3 Overlap area of two circles

A brief consideration is given to the form of $\mathcal{A}(r_1, r_2; \mu)$. In the event the circles completely overlap or do not overlap at all, its evaluation is trivially,

$$\mathcal{A}(r_1, r_2; \mu) = \begin{cases} 0, & \mu \geq r_1 + r_2; \\ \pi \min[r_1^2, r_2^2], & \mu \leq |r_1 - r_2|. \end{cases} \quad (\text{A.42})$$

Otherwise, consider figure 17. The shaded area A_1 is obtained by subtracting the area of the triangle from that of the sector,

$$A_1 = r_1^2 \cos^{-1} \left(\frac{x^*}{r_1} \right) - x^* y^*. \quad (\text{A.43})$$

Similarly,

$$A_2 = r_2^2 \cos^{-1} \left(\frac{r - x^*}{r_2} \right) - (r - x^*) y^*. \quad (\text{A.44})$$

Adding these,

$$\mathcal{A}(r_1, r_2; \mu) = r_1^2 \cos^{-1} \left(\frac{x^*}{r_1} \right) + r_2^2 \cos^{-1} \left(\frac{\mu - x^*}{r_2} \right) - r y^*. \quad (\text{A.45})$$

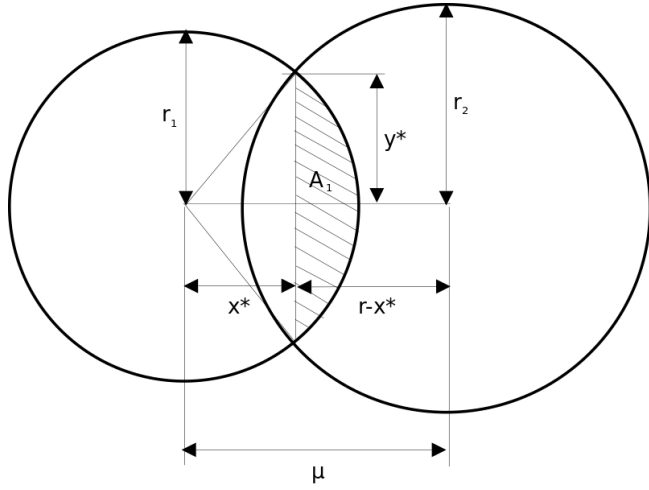


Figure 17: The overlap area of two circles, radii r_1 and r_2 , with a distance μ between their centres.

The values of x^* and y^* are derived by solving the simultaneous equations,

$$r_1^2 = x^{*2} + y^{*2}, \quad (\text{A.46})$$

$$r_2^2 = (x^* + \mu)^2 + y^{*2}, \quad (\text{A.47})$$

to give,

$$x^* = (\mu^2 + r_1^2 - r_2^2)/2\mu, \quad (\text{A.48})$$

$$y^* = \sqrt{[(r_1 + r_2)^2 - \mu^2][\mu^2 - (r_1 - r_2)^2]}/2\mu. \quad (\text{A.49})$$

Hence,

$$\mathcal{A}(r_1, r_2; \mu) = \begin{cases} 0, & \mu \geq r_1 + r_2; \\ \pi \min[r_1^2, r_2^2], & \mu \leq |r_1 - r_2|; \\ r_1^2 \cos^{-1}\left(\frac{\mu^2 + r_1^2 - r_2^2}{2\mu r_1}\right) + r_2^2 \cos^{-1}\left(\frac{\mu^2 + r_2^2 - r_1^2}{2\mu r_2}\right) \\ -\frac{1}{2}[(r_1 + r_2)^2 - \mu^2][\mu^2 - (r_1 - r_2)^2]^{1/2}, & \text{otherwise.} \end{cases} \quad (\text{A.50})$$

A.4 Derivative of \mathcal{A}

It is obvious from (A.16) when $|r_1 - r_2| \geq \mu$ or $\mu \geq r_1 + r_2$ that $d\mathcal{A}(r_1, r_2; \mu) = 0$. By considering where $|r_1 - r_2| \leq \mu \leq r_1 + r_2$ and using the identity,

$$\Upsilon(r_1, r_2; \mu) = [(r_1 + r_2)^2 - \mu^2][\mu^2 - (r_1 - r_2)^2] = -\mu^4 + 2\mu^2(r_1^2 + r_2^2) - (r_1^2 - r_2^2)^2,$$

it can be shown that,

$$\frac{d\mathcal{A}(r_1, r_2; \mu)}{d\mu} = -r_1^2 \left[1 - \left(\frac{\mu^2 + r_1^2 - r_2^2}{2\mu r_1} \right)^2 \right]^{-1/2} \left[\frac{4\mu^2 r_1 - 2r_1(\mu^2 + r_1^2 - r_2^2)}{4r_1^2 \mu^2} \right]$$

$$\begin{aligned}
& - \mu_2^2 \left[1 - \left(\frac{\mu^2 + r_2^2 - r_1^2}{2\mu r_2} \right)^2 \right]^{-1/2} \left[\frac{4\mu^2 r_2 - 2r_2(\mu^2 + r_2^2 - r_1^2)}{4r_2^2 \mu^2} \right] \\
& - \frac{1}{4} [\Upsilon(r_1, r_2; \mu)]^{-1/2} [-4\mu^3 + 4(r_1^2 + r_2^2)\mu], \tag{A.51}
\end{aligned}$$

$$\begin{aligned}
& = -r_1^2 \left[\frac{2\mu^2 r_1 - 2r_1^3 + 2r_1 r_2^2}{2\mu r_1 \sqrt{4\mu^2 r_1^2 - (\mu^2 + r_1^2 - r_2^2)^2}} \right] \\
& - r_2^2 \left[\frac{2\mu^2 r_2 - 2r_2^3 + 2r_2 r_1^2}{2\mu r_2 \sqrt{4\mu^2 r_2^2 - (\mu^2 + r_2^2 - r_1^2)^2}} \right] \\
& - \frac{(r_1^2 + r_2^2)\mu - \mu^3}{\sqrt{\Upsilon(r_1, r_2; \mu)}}, \tag{A.52}
\end{aligned}$$

$$\begin{aligned}
& = -r_1 \left[\frac{2r_1(\mu^2 - r_1^2 + r_2^2)}{2\mu \sqrt{-\mu^4 + 2\mu^2(r_1^2 + r_2^2) - (r_1^2 - r_2^2)^2}} \right] \\
& - r_2 \left[\frac{2r_2(\mu^2 - r_2^2 + r_1^2)}{2\mu \sqrt{-\mu^4 + 2\mu^2(r_1^2 + r_2^2) - (r_1^2 - r_2^2)^2}} \right] \\
& - \frac{(r_1^2 + r_2^2)\mu - \mu^3}{\sqrt{\Upsilon(r_1, r_2; \mu)}}, \tag{A.53}
\end{aligned}$$

$$= -\frac{r_1^2(\mu^2 - r_1^2 + r_2^2)}{\mu \sqrt{\Upsilon(r_1, r_2; \mu)}} - \frac{r_2^2(\mu^2 - r_2^2 + r_1^2)}{\mu \sqrt{\Upsilon(r_1, r_2; \mu)}} - \frac{(r_1^2 + r_2^2)\mu - \mu^3}{\sqrt{\Upsilon(r_1, r_2; \mu)}}, \tag{A.54}$$

$$= -\frac{2\mu^2(r_1^2 + r_2^2) - (r_1^4 + r_2^4 - 2r_1^2 r_2^2) - \mu^4}{\mu \sqrt{\Upsilon(r_1, r_2; \mu)}}, \tag{A.55}$$

$$= -\frac{\sqrt{\Upsilon(r_1, r_2; \mu)}}{\mu}. \tag{A.56}$$

B Common solutions of the lidar equation

B.1 The Klett solution for elastic lidar

The most basic mode of operation for any lidar is its elastic mode. This collects a single profile of the atmosphere, such the backscatter and attenuation coefficients must be derived from a single measurement at each height. As this mode should provide the signal of the greatest magnitude, it is important to be able to analyse it without additional lidar measurements. This is obviously impossible without assuming a relation between the backscatter and attenuation coefficients. The most common of these was first outlined in Klett [1981] and expanded in Klett [1985].

For a vertically-pointing ($R \equiv z$), elastic backscatter lidar ($\lambda_L = \lambda_x \equiv \lambda$), equation (2.14) may be written,

$$z^2 E'(\lambda, z) = E_L(\lambda) \frac{c\tau_d}{2} \eta(\lambda) A(z) \beta(\lambda, z) \exp \left[-2 \int_0^z \alpha(\lambda, z') dz' \right], \tag{B.1}$$

$$S(z) = S_0 + \ln \frac{A(z)}{A(0)} + \ln \frac{\beta(\lambda, z)}{\beta_0} - 2 \int_0^z \alpha(\lambda, z') dz', \tag{B.2}$$

where $S(z) = \ln[z^2 E'(z)]$; $E'(\lambda, z) = E(\lambda, z) - E_B(\lambda)$; and S_0 and β_0 are constants. Differentiating with respect to z and assuming the variation of $A(z)$ is negligible above some limiting height,

$$\frac{dS}{dz} = \frac{1}{\beta} \frac{d\beta}{dz} - 2\alpha. \quad (\text{B.3})$$

The Klett method assumes that when particulate backscattering dominates over molecular scattering,

$$\beta = B^{-1}\alpha^k, \quad (\text{B.4})$$

where the lidar ratio, B , and the Ångstrom coefficient, k , are determined empirically from field studies. As the extinction and backscatter coefficients are integrals over the size distributions of gas molecules and aerosols, this assumption is equivalent to stating that the spectral shape and composition of the scatterers are spatially invariant and any variations in backscatter are due solely to variations in scatterer density.

Using this relation, equation (B.3) can be written as,

$$\frac{dS}{dz} = \frac{k}{\alpha} \frac{d\alpha}{dz} - 2\alpha. \quad (\text{B.5})$$

This is a Bernoulli equation which can be solved by introducing the change of variable $w = \alpha^{-1}$ to give,

$$\alpha = \exp \left[\int \frac{1}{k} \frac{dS}{dz'} dz' \right] \left[C - \int \frac{2}{k} \exp \left[\int \frac{1}{k} \frac{dS}{dz''} dz'' \right] dz \right]^{-1}, \quad (\text{B.6})$$

where C is an integration constant.

Using the obvious boundary condition at $z = 0$ regrettably produces a solution that is not stable to numerical integration and demonstrates an exponential increase in errors with increasing range [Hughes et al., 1985; Klett, 1981]. By instead integrating from a reference range z_m to z , a stable solution is obtained,

$$\alpha(z) = \frac{\exp \left(\frac{S(z) - S(z_m)}{k} \right)}{\alpha(z_m)^{-1} + \frac{2}{k} \int_z^{z_m} \exp \left(\frac{S(z') - S(z_m)}{k} \right) dz'}. \quad (\text{B.7})$$

When using equation B.4, it is common to assume $k = 1$ [Gaumet et al., 1998; Reagan et al., 1989], though the work of Klett [1985] demonstrates that for transitional regions where spectral characteristics are changing it is better to use $k = 1.3$.

B.2 The Ansmann solution for Raman lidar

The nitrogen or oxygen Raman profile alone can be used to derive the extinction coefficient of the atmosphere. As outlined in Ansmann et al. [1990], equation (2.21) is rearranged as,

$$\begin{aligned} \alpha(\lambda_0, R) + \alpha(\lambda_x, R) &= \frac{d}{dR} \left[\ln \frac{N_x(R)}{E'(\lambda_x, R) R^2} \right], \\ \alpha_a(\lambda_0, R) + \alpha_a(\lambda_x, R) &= \frac{d}{dR} \left[\ln \frac{N_x(R)}{E'(\lambda_x, R) R^2} \right] \end{aligned} \quad (\text{B.8})$$

$$-\alpha_m(\lambda_0, R) - \alpha_m(\lambda_x, R), \quad (\text{B.9})$$

where $E'(\lambda_x, z) = E(\lambda_x, z) - E_B(\lambda_x)$.

A wavelength dependence for the aerosol coefficients is assumed,

$$\frac{\alpha_a(\lambda_0, R)}{\alpha_a(\lambda_x, R)} = \left(\frac{\lambda_x}{\lambda_0} \right)^k, \quad (\text{B.10})$$

where $k = 1$ for particles comparable in size to λ and $k = 0$ for larger particles [Ansmann et al., 1992b].

Hence,

$$\alpha_a(\lambda, R) = \frac{\frac{d}{dR} \left[\ln \frac{N_X(R)}{E'(\lambda_x, R)R^2} \right] - \alpha_m(\lambda, R) - \alpha_m(\lambda_x, R)}{1 + (\lambda/\lambda_x)^k}. \quad (\text{B.11})$$

C Levenberg-Marquadt iteration

This work uses the methods outlined in Chapter 7 of Rodgers [2000]. This defines an inverse problem,

$$\mathbf{y} = \mathbf{F}(\mathbf{x}, \mathbf{b}) + \boldsymbol{\varepsilon}, \quad (\text{C.1})$$

which relates the measurement vector, \mathbf{y} , to the state vector, \mathbf{x} , with an error, $\boldsymbol{\varepsilon}$, through the forward model, \mathbf{F} , which uses the known parameters, \mathbf{b} .

The solution, $\hat{\mathbf{x}}$, with the maximal probability of representing the true state of the atmosphere, given the measurements, known as the maximum *a posteriori* solution, is sought. This can be found by using Bayesian statistics and assuming the probability density functions describing all quantities are Gaussian (or at least symmetric). In such circumstances,

$$-2 \ln P(\mathbf{y}|\mathbf{x}) = [\mathbf{y} - \mathbf{F}(\mathbf{x}, \mathbf{b})]^T \mathbf{S}_\varepsilon^{-1} [\mathbf{y} - \mathbf{F}(\mathbf{x}, \mathbf{b})] + c_1, \quad (\text{C.2})$$

where c_1 is a constant; $\mathbf{S}_\varepsilon^{-1} = \langle [\mathbf{y} - \mathbf{F}(\mathbf{x}, \mathbf{b})][\mathbf{y} - \mathbf{F}(\mathbf{x}, \mathbf{b})]^T \rangle$ is the error covariance of the measurement; and $P(\mathbf{x})$ stands for the probability of observing a state \mathbf{x} . The prior knowledge of the system is summarised by an *a priori* state vector, \mathbf{x}_a , which, though not necessarily realistic, is also modelled with a symmetric probability density function such that,

$$-2 \ln P(\mathbf{x}) = [\mathbf{x} - \mathbf{x}_a]^T \mathbf{S}_a^{-1} [\mathbf{x} - \mathbf{x}_a] + c_2, \quad (\text{C.3})$$

where \mathbf{S}_a^{-1} is the covariance matrix of the *a priori*.

Substituting these into Bayes' Theorem,

$$P(\mathbf{x}|\mathbf{y}) = \frac{P(\mathbf{y}|\mathbf{x})P(\mathbf{x})}{P(\mathbf{y})}, \quad (\text{C.4})$$

gives the cost function,

$$-2 \ln P(\mathbf{x}|\mathbf{y}) = [\mathbf{y} - \mathbf{F}(\mathbf{x}, \mathbf{b})]^T \mathbf{S}_\varepsilon^{-1} [\mathbf{y} - \mathbf{F}(\mathbf{x}, \mathbf{b})] + [\mathbf{x} - \mathbf{x}_a]^T \mathbf{S}_a^{-1} [\mathbf{x} - \mathbf{x}_a] + c_3, \quad (\text{C.5})$$

where it has been assumed that $P(\mathbf{y})$ is a normalising constant.

The maximum probability state, $\hat{\mathbf{x}}$, is found by equating the derivative of (C.5) to zero,

$$0 = \nabla_{\mathbf{x}} \{-2 \ln[\text{P}(\mathbf{x}|\mathbf{y})]\} = -[\nabla_{\mathbf{x}} \mathbf{F}(\mathbf{x}, \mathbf{b})]^T \mathbf{S}_{\varepsilon}^{-1} [\mathbf{y} - \mathbf{F}(\mathbf{x}, \mathbf{b})] + \mathbf{S}_a^{-1} [\mathbf{x} - \mathbf{x}_a]. \quad (\text{C.6})$$

Defining $\mathbf{K}(\mathbf{x}) = \nabla_{\mathbf{x}} \mathbf{F}(\mathbf{x}, \mathbf{b})$,

$$-\mathbf{K}^T(\hat{\mathbf{x}}) \mathbf{S}_{\varepsilon}^{-1} [\mathbf{y} - \mathbf{F}(\hat{\mathbf{x}}, \mathbf{b})] + \mathbf{S}_a^{-1} [\hat{\mathbf{x}} - \mathbf{x}_a] = 0. \quad (\text{C.7})$$

For a quasi-linear problem, a straightforward Newton iteration can be used. It states that for the general vector equation $\mathbf{g}(\mathbf{x}) = 0$, the solution can be found by the iteration,

$$\mathbf{x}_{i+1} = \mathbf{x}_i - [\nabla_{\mathbf{x}} \mathbf{g}(\mathbf{x}_i)]^{-1} \mathbf{g}(\mathbf{x}_i). \quad (\text{C.8})$$

Hence, to solve equation (C.7),

$$\mathbf{g} = -\mathbf{K}^T(\hat{\mathbf{x}}) \mathbf{S}_{\varepsilon}^{-1} [\mathbf{y} - \mathbf{F}(\hat{\mathbf{x}}, \mathbf{b})] + \mathbf{S}_a^{-1} [\hat{\mathbf{x}} - \mathbf{x}_a], \quad (\text{C.9})$$

$$\nabla_{\mathbf{x}} \mathbf{g} = \mathbf{S}_a^{-1} + \mathbf{K}^T \mathbf{S}_{\varepsilon}^{-1} \mathbf{K} - [\nabla_{\mathbf{x}} \mathbf{K}^T] \mathbf{S}_{\varepsilon}^{-1} [\mathbf{y} - \mathbf{F}(\mathbf{x}, \mathbf{b})]. \quad (\text{C.10})$$

For the quasi-linear case the last term of (C.10) is neglected, giving the Gauss-Newton iteration,

$$\mathbf{x}_{i+1} = \mathbf{x}_i + (\mathbf{S}_a^{-1} + \mathbf{K}_i^T \mathbf{S}_{\varepsilon}^{-1} \mathbf{K}_i)^{-1} \{ \mathbf{K}_i^T \mathbf{S}_{\varepsilon}^{-1} [\mathbf{y} - \mathbf{F}(\mathbf{x}_i, \mathbf{b})] - \mathbf{S}_a^{-1} (\mathbf{x}_i - \mathbf{x}_a) \}.$$

However, if the forward model is not necessarily quasi-linear, the last term of (C.10) is instead approximated by $\gamma_i \mathbf{S}_a^{-1}$, where γ_i is chosen at each step to reduce the cost function (C.5). This is known as the Levenberg–Marquardt method,

$$\mathbf{x}_{i+1} = \mathbf{x}_i + [(1 + \gamma_i) \mathbf{S}_a^{-1} + \mathbf{K}_i^T \mathbf{S}_{\varepsilon}^{-1} \mathbf{K}_i]^{-1} \{ \mathbf{K}_i^T \mathbf{S}_{\varepsilon}^{-1} [\mathbf{y} - \mathbf{F}(\mathbf{x}_i, \epsilon)] - \mathbf{S}_a^{-1} (\mathbf{x}_i - \mathbf{x}_a) \}.$$

General practice is that after an iteration, if the cost has increased, γ_i is increased by a factor of ten. Otherwise, it is reduced by a factor of two. Iteration ceases when either the cost function or all elements of the state vector change by less than some threshold after a step.

D Cubic spline interpolation

The forward model uses the cubic spline scheme outlined in Press et al. [1992, Section 3.3] to interpolate the backscatter and AOT from the state vector's coarse vertical axis, R , onto the measurement vector's finer axis, z . In this scheme, the backscatter at an arbitrary point, $\beta(z_i)$, may be expressed in terms of the backscatter on the state vector axis just below and above this point, $\beta(R_j) \equiv \beta_j$ and $\beta(R_{j+1}) \equiv \beta_{j+1}$ respectively, and their second derivatives as,

$$\beta(z_i) = A_{ij} \beta_j + B_{ij} \beta_{j+1} + C_{ij} \beta''_j + D_{ij} \beta''_{j+1}, \quad (\text{D.1})$$

where,

$$A_{ij} = \frac{R_{j+1} - z_i}{R_{j+1} - R_j}; \quad B_{ij} = 1 - A_{ij};$$

$$C_{ij} = \frac{(A_{ij}^3 - A_{ij})(R_{j+1} - R_j)^2}{6}; \quad D_{ij} = \frac{(B_{ij}^3 - B_{ij})(R_{j+1} - R_j)^2}{6}.$$

By requiring that $\beta(R)$ has a continuous first derivative, it can be shown that,

$$\frac{R_j - R_{j-1}}{6}\beta''_{j-1} + \frac{R_{j+1} - R_{j-1}}{3}\beta''_j + \frac{R_{j+1} - R_j}{6}\beta''_{j+1} = \frac{\beta_{j+1} - \beta_j}{R_{j+1} - R_j} - \frac{\beta_j - \beta_{j-1}}{R_j - R_{j-1}}. \quad (\text{D.2})$$

This represents a set of $N - 2$ equations, where N is the number of points on the state vector axis. This is solved using standard linear algebra routines and the constraint,

$$\beta''_0 = \beta''_{N-1} = 0. \quad (\text{D.3})$$

E Forward model derivatives

By defining a state vector,

$$\boldsymbol{x} = [\boldsymbol{\beta}, \boldsymbol{\alpha}], \quad (\text{E.1})$$

and a measurement vector,

$$\boldsymbol{y} = [\boldsymbol{n}_{\text{el}}^F, \boldsymbol{n}_{\text{ra}}^F], \quad (\text{E.2})$$

the K matrix will consist of four sections — $\mathbf{K}^{\beta, \text{el}}$, $\mathbf{K}^{\beta, \text{ra}}$, $\mathbf{K}^{\alpha, \text{el}}$, and $\mathbf{K}^{\alpha, \text{ra}}$.

E.1 Backscatter

For the calculation of the backscatter component of the forward model's \mathbf{K} matrix using the cubic spline scheme, it is evident from equation (D.1) that,

$$K_{ki}^{(\beta)} \propto \frac{\partial \beta(z_i)}{\partial \beta_k} = A_{ij}\delta_{jk} + B_{ij}\delta_{(j+1)k} + C_{ij}\frac{\partial \beta''_j}{\partial \beta_k} + D_{ij}\frac{\partial \beta''_{j+1}}{\partial \beta_k}, \quad (\text{E.3})$$

where $0 \leq k \leq N - 1$ and δ_{ab} is a delta function.

By (D.3), for $j = 0$ the third term disappears, as does the final term for $j = N - 1$. To evaluate these terms for arbitrary j , note that (D.2) is a series of linear equations of the form,

$$\mathbf{E}\boldsymbol{\beta}'' = \mathbf{F}\boldsymbol{\beta}, \quad (\text{E.4})$$

where the non-zero terms of E and F are,

$$E_{(i-1)i} = \frac{R_i - R_{i-1}}{6}; \quad E_{ii} = \frac{R_{i+1} - R_{i-1}}{3}; \quad E_{(i+1)i} = \frac{R_{i+1} - R_i}{6};$$

$$F_{(i-1)i} = \frac{1}{R_i - R_{i-1}}; \quad F_{ii} = -\frac{R_{i+1} - R_{i-1}}{(R_{i+1} - R_i)(R_i - R_{i-1})}; \quad F_{(i+1)i} = \frac{1}{R_{i+1} - R_i},$$

for $1 \leq i \leq N - 2$.

Hence, assuming \mathbf{E} is invertible,

$$\beta''_j = \sum_{k=1}^N (\mathbf{E}^{-1}\mathbf{F})_{jk} \beta_k, \quad (\text{E.5})$$

$$\Rightarrow \frac{\partial \beta''_j}{\partial \beta_k} = (\mathbf{E}^{-1} \mathbf{F})_{jk}. \quad (\text{E.6})$$

Thus,

$$\frac{\partial \beta(z_i)}{\partial \beta_k} = \begin{cases} \frac{A_{ij}\delta_{j0} + B_{ij}\delta_{(j+1)0} + D_{ij}(\mathbf{E}^{-1}\mathbf{F})_{(j+1)0},}{A_{ij}\delta_{j(N-1)} + B_{ij}\delta_{(j+1)(N-1)}} & k = 0; \\ \frac{+C_{ij}(\mathbf{E}^{-1}\mathbf{F})_{j(N-1)}}{A_{ij}\delta_{jk} + B_{ij}\delta_{(j+1)k} + C_{ij}(\mathbf{E}^{-1}\mathbf{F})_{jk}} & k = N - 1; \\ +D_{ij}(\mathbf{E}^{-1}\mathbf{F})_{(j+1)k}, & \text{otherwise.} \end{cases} \quad (\text{E.7})$$

The elements of the \mathbf{K}^β matrix can then be determined from,

$$K_{ki}^{\beta, \text{el}} = v_{\text{el}}(R_i) A(R_i, \epsilon) \exp[-2\chi_i] \frac{\partial \beta(z_i)}{\partial \beta_k}, \quad (\text{E.8})$$

$$K_{ki}^{\beta, \text{ra}} = 0. \quad (\text{E.9})$$

E.2 Extinction

As summarised by equation (3.6), the forward model integrates the extinction, $\alpha(R_l) \equiv \alpha_l$, by a simple trapezium rule scheme to determine the AOT, $\chi(R_l) \equiv \chi_l$. This is then interpolated with the cubic spline algorithm onto the measurement's vertical axis. Considering the total derivative,

$$\begin{aligned} d\chi(z_i) &= \sum_{l=0}^{N-1} \frac{\partial \chi(z_i)}{\partial \chi(R_l)} d\chi(R_l) = \sum_{l=0}^{N-1} \frac{\partial \chi(z_i)}{\partial \alpha(R_l)} d\alpha(R_l), \\ &\equiv \sum_{l=0}^{N-1} \frac{\partial \chi(z_i)}{\partial \chi_l} d\chi_l \end{aligned} \quad (\text{E.10})$$

As $\chi(z_i)$ is interpolated from the values χ_l , the terms $\frac{\partial \chi(z_i)}{\partial \chi_l}$ are identical those described in (E.7) for β . Further, the terms $\frac{\partial \chi(z_i)}{\partial \alpha(R_l)}$ are proportional to the terms of the \mathbf{K} matrix.

Hence, dividing both sides of (E.10) by $d\alpha_k$,

$$K_{ki}^{(\alpha)} \propto \frac{\partial \chi(z_i)}{\partial \alpha_k} = \sum_{l=0}^{N-1} \frac{\partial \chi(z_i)}{\partial \chi_l} \frac{\partial \chi_l}{\partial \alpha_k}. \quad (\text{E.11})$$

By (3.6), for $0 \leq l \leq N - 1$,

$$\chi_l = \begin{cases} R_0 \alpha_0, & l = 0; \\ R_0 \alpha_0 + \sum_{m=1}^l \frac{1}{2}(\alpha_m + \alpha_{m-1})(R_m - R_{m-1}), & \text{otherwise.} \end{cases} \quad (\text{E.12})$$

Hence,

$$\frac{d\chi_l}{d\alpha_k} = \begin{cases} 0, & l < k; \\ \frac{1}{2}(R_k - R_{k-1}), & l = (k \neq 0); \\ \frac{1}{2}(R_{k+1} - R_{k-1}), & l > (k \neq 0); \\ \frac{1}{2}(R_1 + R_0), & l > (k = 0); \\ R_0, & l = k = 0. \end{cases} \quad (\text{E.13})$$

Substituting this and (E.7) into (E.11),

$$\frac{\partial \chi(z_i)}{\partial \alpha_k} = \begin{cases} \frac{1}{2}(R_{N-1} - R_{N-2}) \frac{\partial \chi(z_i)}{\partial \chi_{N-1}}, & k = N-1; \\ \frac{1}{2}(R_k - R_{k-1}) \frac{\partial \chi(z_i)}{\partial \chi_k} \\ + \frac{1}{2}(R_{k+1} - R_{k-1}) \sum_{l=k+1}^{N-1} \frac{\partial \chi(z_i)}{\partial \chi_l}, & 0 < k < N-1; \\ R_0 \frac{\partial \chi(z_i)}{\partial \chi_0} + \frac{1}{2}(R_1 - R_0) \sum_{l=1}^{N-1} \frac{\partial \chi(z_i)}{\partial \chi_l}, & k = 0, \end{cases} \quad (\text{E.14})$$

where the partial derivatives are defined in (E.7).

The elements of the \mathbf{K}^α matrix can then be determined from,

$$K_{ki}^{\alpha, \text{el}} = -2n_{\text{el}}(R_i) \frac{\partial \chi(z_i)}{\partial \alpha_k}, \quad (\text{E.15})$$

$$K_{ki}^{\alpha, \text{ra}} = -\left(1 + \frac{\lambda_L}{\lambda_X}\right) n_{\text{ra}}(R_i) \frac{\partial \chi(z_i)}{\partial \alpha_k}. \quad (\text{E.16})$$

E.3 PMT correction

The correction for the non-linearity of the PMT will change the columns of the \mathbf{K} matrix as,

$$K_{ki}^{*, \text{el}} = \frac{K_{ki}^{\text{el}}}{\left(1 + \frac{n_{\text{el}}(z_k)}{n_0} \frac{\tau_P^{(\text{el})}}{\tau_d}\right)^2}, \quad (\text{E.17})$$

$$K_{ki}^{*, \text{re}} = \frac{K_{ki}^{\text{re}}}{\left(1 + \frac{n_{\text{re}}(z_k)}{n_0} \frac{\tau_P^{(\text{re})}}{\tau_d}\right)^2}. \quad (\text{E.18})$$

E.4 Overlap function

The parameter retrieval scheme of Section 3.3.2 requires derivatives of the overlap function derived in Appendix A with respect to ϵ . As equation (3.8) is evaluated using numerical integration, the derivatives of \mathbf{y} with respect to the elements of ϵ will also require some numerical integration.

E.4.1 With respect to d

The parameters δ , ϕ_{\parallel} , and ϕ_{\perp} only enter the expression for $A(R)$ through the variable d . Hence, we consider,

$$\frac{\partial A(z_i)}{\partial d} = \left(\frac{\gamma}{\nu w}\right)^2 \left[\left| \frac{\partial S_H}{\partial d} \right|_{z_i, \frac{\nu}{\gamma} R_T} - \left| \frac{\partial S_H}{\partial d} \right|_{z_i, \frac{\nu}{\gamma} R_o} \right], \quad (\text{E.19})$$

where,

$$\left| \frac{\partial S_H}{\partial d} \right|_{z_i, \rho} = \begin{cases} 0, & \alpha + \rho \leq d - w \\ & \text{or } w + d \leq |\alpha - \rho| \\ & \text{or } \alpha + \rho \leq w - d; \\ \frac{\int_{\min[w+d, \alpha+\rho]}^{\max[|w-d|, |\alpha-\rho|]} \sqrt{\Upsilon(\alpha, \rho; \mu) \Upsilon(\mu, w; d)}}{\pi \mu d} d\mu, & \text{otherwise,} \end{cases}$$

where the derivatives of $\mathbb{A}(\alpha, \rho; w + d)$ and \mathbb{B} cancelled with those of the limits of the integral.

Hence,

$$K_{1i}^{\text{el|ra}} = \frac{n_{\text{el|ra}}}{A(z_i, \epsilon)} \frac{\partial A(z_i, \epsilon)}{\partial d_i} \frac{\delta + \phi_{\parallel} z_i}{d_i}, \quad (\text{E.20})$$

$$K_{2i}^{\text{el|ra}} = \frac{n_{\text{el|ra}}}{A(z_i, \epsilon)} \frac{\partial A(z_i, \epsilon)}{\partial d_i} \frac{(\delta + \phi_{\parallel} z_i) z_i}{d_i}, \quad (\text{E.21})$$

$$K_{3i}^{\text{el|ra}} = \frac{n_{\text{el|ra}}}{A(z_i, \epsilon)} \frac{\partial A(z_i, \epsilon)}{\partial d_i} \frac{\phi_{\perp} z_i^2}{d_i}. \quad (\text{E.22})$$

E.4.2 With respect to Δ

The derivative with respect to Δ is more involved, as Δ enters the overlap function in both γ and ν . Here,

$$\frac{\partial \gamma}{\partial \Delta} \equiv \gamma'' = \frac{1}{f}, \quad (\text{E.23})$$

$$\frac{\partial \nu}{\partial \Delta} \equiv \nu'' = \text{sign}(\nu) \left[\gamma'' - \frac{z_i}{f^2} \right], \quad (\text{E.24})$$

$$\frac{\partial \alpha}{\partial \Delta} \equiv \alpha'' = -\frac{R_a z_i}{f \gamma^2} \gamma'', \quad (\text{E.25})$$

$$\frac{\partial \rho_x}{\partial \Delta} \equiv \rho_x'' = R_x \left[\frac{\nu''}{\gamma} - \frac{\nu \gamma''}{\gamma^2} \right]. \quad (\text{E.26})$$

Thus,

$$\begin{aligned} \frac{\partial A(z_i)}{\partial \Delta} &= \left(\frac{\gamma}{\nu w} \right)^2 \left[\left| \frac{\partial S_H}{\partial \Delta} \right|_{z_i, \frac{\nu}{\gamma} R_T} - \left| \frac{\partial S_H}{\partial \Delta} \right|_{z_i, \frac{\nu}{\gamma} R_o} \right. \\ &\quad \left. + 2 \left[S_H \left(z_i, \frac{\nu}{\gamma} R_T \right) - S_H \left(z_i, \frac{\nu}{\gamma} R_o \right) \right] \left(\frac{\gamma''}{\gamma} - \frac{\nu''}{\nu} \right) \right], \end{aligned} \quad (\text{E.27})$$

where, integrating $\int \frac{d}{d\Delta} \sqrt{\Upsilon(\alpha, \rho; \mu)} \mathbb{A}(\mu, w; d) \frac{d\mu}{\mu}$ by parts in order to avoid a

pole in the integrand for numerical evaluation,

$$\begin{aligned}
\left| \frac{\partial S_H}{\partial \Delta} \right|_{z_i, \rho} &= \begin{cases} 0, & \alpha + \rho \leq d - w; \\ 2\pi w^2 \varsigma, & w + d \leq |\alpha - \rho| \\ 2\pi \alpha \rho (\alpha'' \rho + \alpha \rho''), & \alpha + \rho \leq w - d; \\ \pi \varsigma [\mathbb{A}(\alpha + \rho, w; d) + \mathbb{A}(|\alpha - \rho|, w; d)] \\ - \int_{|\alpha-\rho|}^{\alpha+\rho} \mathbb{D}(\rho, \mu) d\mu, & \alpha + \rho \leq w + d \\ \text{and } |w - d| \leq |\alpha - \rho|; \\ \pi \varsigma \mathbb{A}(\alpha + \rho, w; d) - \int_{d-w}^{\alpha+\rho} \mathbb{D}(\rho, \mu) d\mu, & \alpha + \rho \leq w + d \\ \text{and } |\alpha - \rho| < d - w; \\ \pi \varsigma \mathbb{A}(\alpha + \rho, w; d) - (w - d)^2 \mathbb{E}(w - d) \\ + \mathbb{B}'' - \int_{w-d}^{\alpha+\rho} \mathbb{D}(\rho, \mu) d\mu, & \alpha + \rho \leq w + d \\ \text{and } |\alpha - \rho| < w - d; \\ w^2 [\mathbb{A}'' + \mathbb{E}(w + d)] + \pi \varsigma \mathbb{A}(|\alpha - \rho|, w; d) \\ - \int_{|\alpha-\rho|}^{w+d} \mathbb{D}(\rho, \mu) d\mu, & w + d < \alpha + \rho \\ \text{and } |w - d| \leq |\alpha - \rho|; \\ w^2 [\mathbb{A}'' + \mathbb{E}(w + d)] - \int_{d-w}^{w+d} \mathbb{D}(\rho, \mu) d\mu, & w + d < \alpha + \rho \\ \text{and } |\alpha - \rho| < w - d \\ w^2 [\mathbb{A}'' + \mathbb{E}(w + d)] - (w - d)^2 \mathbb{E}(w - d) \\ + \mathbb{B}'' - \int_{w-d}^{w+d} \mathbb{D}(\rho, \mu) d\mu, & w + d < \alpha + \rho \\ \text{and } |\alpha - \rho| < w - d, \end{cases} \\
\varsigma &= \begin{cases} \alpha \alpha'', & \alpha < \rho; \\ \rho \rho'', & \alpha > \rho, \end{cases} \\
\mathbb{A}'' &= 2 \left[\alpha \alpha'' \cos^{-1} \frac{(w + d)^2 + \alpha^2 - \rho^2}{2(w + d)\alpha} + \rho \rho'' \cos^{-1} \frac{(w + d)^2 - \alpha^2 + \rho^2}{2(w + d)\rho} \right] \\
\mathbb{B}'' &= 4\alpha\rho(\rho\alpha'' + \alpha\rho'') \tan^{-1} \sqrt{\frac{(w - d)^2 - (\alpha - \rho)^2}{(\alpha + \rho)^2 - (w - d)^2}} \\
&\quad - \sqrt{\Upsilon(\alpha, \rho; w - d)}(\alpha\alpha'' + \rho\rho''), \\
\mathbb{D}(\rho, \mu) &= \frac{2\mu}{\pi} \mathbb{E}(\mu) \cos^{-1} \frac{d^2 + \mu^2 - w^2}{2d\mu}, \\
\mathbb{E}(\mu) &= (\alpha\alpha'' + \rho\rho'') \tan^{-1} \left[\frac{\mu^2 - \alpha^2 - \rho^2}{\sqrt{\Upsilon(\alpha, \rho; \mu)}} \right] \\
&\quad + (\alpha\alpha'' - \rho\rho'') \tan^{-1} \left[\frac{\alpha^4 + \rho^4 - \mu^2(\alpha^2 + \rho^2) - 2\alpha^2\rho^2}{(\alpha^2 - \rho^2)\sqrt{\Upsilon(\alpha, \rho; \mu)}} \right],
\end{aligned}$$

where $\mathbb{E}(\mu) = \int \frac{d}{d\Delta} \sqrt{\Upsilon(\alpha, \rho, \mu)} \frac{d\mu}{\mu}$ and the identities $\mathbb{A}(w + d, w; d) = w^2$, $\mathbb{A}(w - d, w; d) = (w - d)^2$ and,

$$\mathbb{E}(\alpha + \rho) = -\mathbb{E}(|\alpha - \rho|) = \begin{cases} \pi \alpha \alpha'', & \alpha < \rho; \\ \pi \rho \rho'', & \alpha > \rho, \end{cases}$$

have been used.

Hence,

$$K_{0i}^{\text{el}| \text{ra}} = \frac{n_{\text{el}| \text{ra}}}{A(z_i, \epsilon)} \frac{\partial A(z_i, \epsilon)}{\partial \Delta}. \quad (\text{E.28})$$

References

- Agnew, J. (2003). Lidar and radar tropospheric profiling at Chilbolton Observatory. During *Sixth International Symposium on Tropospheric Profiling: Needs and Technologies*, pages 151–153.
- Agnew, J. and Wrench, C. (2006 – 2010). Chilbolton UV Raman lidar raw data. STFC Chilbolton Observatory, Rutherford Appleton Laboratory.
- Althausen, D., Muller, D., Ansmann, A., Wandinger, U., Hube, H., Clauder, E., and Zorner, S. (2000). Scanning 6-wavelength 11-channel aerosol lidar. *Journal of Atmospheric and Oceanic Technology*, 17(11):1469–1482. ISI Document Delivery No.: 377LR Times Cited: 84 Cited Reference Count: 70 Althausen, D Muller, D Ansmann, A Wandinger, U Hube, H Clauder, E Zorner, S AMER METEOROLOGICAL SOC BOSTON.
- Amodeo, A., Mattis, I., Boeckmann, C., D'Amico, G., Mueller, D., Osterloh, L., Chaikovsky, A., Pappalardo, G., Ansmann, A., Apituley, A., Alados-Arboledas, L., Balis, D., Comeron, A., Freudenthaler, V., Mitev, V., Nicolae, D., Papayannis, A., Perrone, M. R., Pietruezuk, A., Pujadas, M., Putaud, J. P., Ravetta, F., Rizi, V., Simeonovs, V., Spinelli, N., Stebel, K., Stoyanov, D., Trickl, T., and Wiegner, M. (2009). Optimization of lidar data processing: A goal of the EARLINET-ASOS project. During *Conference on Lidar Technologies, Techniques, and Measurements for Atmospheric Remote Sensing III*, editors: Singh, U. N. and Pappalardo, G., volume 6750, pages F7500–F7500.
- Ansmann, A., Riebesell, M., Wandinger, U., Weitkamp, C., Voss, E., Lahmann, W., and Michaelis, W. (1992a). Combined Raman elastic-backscatter lidar for vertical profiling of moisture, aerosol extinction, backscatter, and lidar ratio. *Applied Physics B — Photophysics and Laser Chemistry*, 55(1):18–28.
- Ansmann, A., Riebesell, M., and Weitkamp, C. (1990). Measurement of atmospheric aerosol extinction profiles with a Raman lidar. *Optics Letters*, 15(13):746–748.
- Ansmann, A., Wandinger, U., Riebesell, M., Weitkamp, C., and Michaelis, W. (1992b). Independent measurement of extinction and backscatter profiles in cirrus clouds by using a combined Raman elastic-backscatter lidar. *Applied Optics*, 31(33):7113–7131.
- Argall, P. and Sica, R. (2003). *Lidar: Atmospheric sounding introduction*, pages 1169–1176. Academic Press, San Diego, CA.
- Biavati, G. (2011). personal communication. Max Planck Institute (Biogeochemie), Jena, Germany.
- Bockmann, C., Wandinger, U., Ansmann, A., Bosenberg, J., Amiridis, V., Boselli, A., Delaval, A., De Tomasi, F., Frioud, M., Grigorov, I. V., Haggard, A., Horvat, M., Iarlori, M., Komguem, L., Kreipl, S., Larchevque, G., Matthias, V., Papayannis, A., Pappalardo, G., Rocadenbosch, F., Rodrigues, J. A., Schneider, J., Shcherbakov, V., and Wiegner, M. (2004). Aerosol lidar intercomparison in the framework of the EARLINET project. 2. Aerosol backscatter algorithms. *Applied Optics*, 43(4):977–989.

- Bucholtz, A. (1995). Rayleigh-scattering calculations for the terrestrial atmosphere. *Applied Optics*, 34(15):2765–2773.
- Bulgin, C. E., Palmer, P. I., Thomas, G. E., Arnold, C. P. G., Campmany, E., Carboni, E., Grainger, R. G., Poulsen, C., Siddans, R., and Lawrence, B. N. (2008). Regional and seasonal variations of the Twomey indirect effect as observed by the ATSR-2 satellite instrument. *Geophysical Research Letters*, 35(2):6.
- Collis, R. T. H. (1966). Lidar — a new atmospheric probe. *Quarterly Journal of the Royal Meteorological Society*, 92(392):220–230.
- Delanoe, J. and Hogan, R. J. (2008). A variational scheme for retrieving ice cloud properties from combined radar, lidar, and infrared radiometer. *Journal of Geophysical Research — Atmospheres*, 113(D7):21.
- Di Girolamo, P., Ambrico, P. F., Amodeo, A., Boselli, A., Pappalardo, G., and Spinelli, N. (1999). Aerosol observations by lidar in the nocturnal boundary layer. *Applied Optics*, 38(21):4585–4595.
- Eloranta, E. W. (1998). Practical model for the calculation of multiply scattered lidar returns. *Applied Optics*, 37(12):2464–2472.
- Fernald, F., Herman, B., and Reagan, J. (1972). Determination of aerosol height distributions by lidar. *Journal of Applied Meteorology*, 11:482–489.
- Ferrare, R. A., Melfi, S. H., Whiteman, D. N., Evans, K. D., Schmidlin, F. J., and Starr, D. O. (1995). A comparison of water-vapor measurements made by Raman lidar and radiosondes. *Journal of Atmospheric and Oceanic Technology*, 12(6):1177–1195.
- Friedland, S. S., Katzenstein, J., and Zatzick, M. R. (1956). Pulsed searchlighting the atmosphere. *Journal of Geophysical Research*, 61(3):415–434.
- Fujii, T. and Fukuchi, T. (2005). *Laser remote sensing*. Taylor and Francis, Boca Raton, FL. Chapter 1.
- Gaumet, J. L., Heinrich, J. C., Cluzeau, M., Pierrard, P., and Prieur, J. (1998). Cloud-base height measurements with a single-pulse erbium-glass laser ceilometer. *Journal of Atmospheric and Oceanic Technology*, 15(1):37–45.
- Goldsmith, J. E. M., Blair, F. H., Bisson, S. E., and Turner, D. D. (1998). Turnkey Raman lidar for profiling atmospheric water vapor, clouds, and aerosols. *Applied Optics*, 37(21):4979–4990.
- Grant, W. B. (1991). Differential absorption and Raman lidar for water-vapor profile measurements — A review. *Optical Engineering*, 30(1):40–48.
- Gross, M. R., McGee, T. J., Singh, U. N., and Kimvilakani, P. (1995). Measurements of stratospheric aerosols with a combined elastic Raman backscatter lidar. *Applied Optics*, 34(30):6915–6924.

- Guerrero-Rascado, J. L., Ruiz, B., Chourdakis, G., Georgoussis, G., and Alados-Arboledas, L. (2008). One year of water vapour Raman lidar measurements at the Andalusian Centre for Environmental Studies (CEAMA). *International Journal of Remote Sensing*, 30:5437–5453.
- Halldórsson, T. and Langerholc, J. (1978). Geometrical form factors for the lidar function. *Applied Optics*, 17(2):240–244.
- He, Q. S., Li, C. C., Mao, J. T., Lau, A. K. H., and Chu, D. A. (2008). Analysis of aerosol vertical distribution and variability in Hong Kong. *Journal of Geophysical Research — Atmospheres*, 113(D14):13.
- Hogan, R. J. (2008). Fast lidar and radar multiple-scattering models. Part I: Small-angle scattering using the photon variance-covariance method. *Journal of the Atmospheric Sciences*, 65(12):3621–3635.
- Hughes, H. G., Ferguson, J. A., and Stephens, D. H. (1985). Sensitivity of a lidar inversion algorithm to parameters relating atmospheric backscatter and extinction. *Applied Optics*, 24(11):1609–1613.
- Hulbert, E. O. (1937). Observations of a searchlight beam to an altitude of 28 kilometers. *Journal of the Optical Society of America*, 27(11):377–382.
- Intergovernmental Panel on Climate Change (IPCC), Solomon, S., Qin, D., Manning, M., Chen, Z., Marquis, M., Averyt, K. B., Tignor, M., and Miller, H. L. (2007). *Climate Change 2007: The Physical Basis of Climate Change. Contribution of Working Group I to the Fourth Assessment Report of the Intergovernmental Panel on Climate Change*. Cambridge University Press, New York.
- King, L. (1923). On the complex anisotropic molecule in relation to the dispersion and scattering of light. *Proceedings of the Royal Society A*, 104:333–357.
- Klett, J. D. (1981). Stable analytical inversion solution for processing lidar returns. *Applied Optics*, 20(2):211–220.
- Klett, J. D. (1985). Lidar inversion with variable backscatter extinction ratios. *Applied Optics*, 24(11):1638–1643.
- Koren, I., Kaufman, Y. J., Rosenfeld, D., Remer, L. A., and Rudich, Y. (2005). Aerosol invigoration and restructuring of Atlantic convective clouds. *Geophysical Research Letters*, 32(14):4.
- Kovalev, V. A., Hao, W. M., and Wold, C. (2007). Determination of the particulate extinction-coefficient profile and the column-integrated lidar ratios using the backscatter-coefficient and optical-depth profiles. *Applied Optics*, 46(36):8627–8634.
- Leblanc, T. and McDermid, I. S. (2008). Accuracy of Raman lidar water vapor calibration and its applicability to long-term measurements. *Applied Optics*, 47(30):5592–5603.
- Lohmann, U. and Feichter, J. (2005). Global indirect aerosol effects: a review. *Atmospheric Chemistry and Physics*, 5:715–737.

- Mattis, I., Muller, D., Ansmann, A., Wandinger, U., Preissler, J., Seifert, P., and Tesche, M. (2008). Ten years of multiwavelength Raman lidar observations of free-tropospheric aerosol layers over central Europe: Geometrical properties and annual cycle. *Journal of Geophysical Research — Atmospheres*, 113(D20).
- Maurya, R., Dubey, P. K., Arya, B. C., and Jain, S. L. (2010). Aerosol vertical profile measurements using micro pulse lidar at New Delhi, India. During *International Symposium for the Advancement of Remote Sensing of the Boundary Layer*.
- Measures, R. M. (1992). *Lidar Remote Sensing: Fundamentals and Applications*. Krieger Publishing Company, Malabar, Florida, second edition.
- National Oceanic and Atmospheric Administration (NOAA) (1976). U.S. Standard Atmosphere. Technical Report NOAA Doc. S/T 76-1562, U.S. Government Printing Office.
- Nedeljkovic, D., Hauchecorne, A., and Chanin, M. L. (1993). Rotational Raman lidar to measure the atmospheric temperature from the ground to 30 km. *IEEE Transactions on Geoscience and Remote Sensing*, 31(1):90–101.
- Nicolae, D., Talianu, C., Radu, C., and Stefan, S. (2007). Combining OPAC and lidar. During *Conference on Lidar Technologies, Techniques, and Measurements for Atmospheric Remote Sensing III*, editors: Singh, U. N. and Pappalardo, G., volume 6750, pages H7500–H7500.
- Oke, T. R. (1987). *Boundary Layer Climates*. Cambridge University Press, second edition.
- Platt, C. M. R. (1981). Remote sounding of high clouds. 3. Monte-Carlo calculations of multiple-scattered lidar returns. *Journal of the Atmospheric Sciences*, 38(1):156–167.
- Povey, A., Grainger, R., Peters, D., Agnew, J., Wrench, C., and Rees, D. (2011). Impact of clouds on aerosol scattering as observed by lidar. During *EGU General Assembly*, Vienna, Austria.
- Press, W. H., Vetterling, W. T., Teukolsky, S. A., and Flannery, B. P. (1992). *Numerical Recipes in C: The Art of Scientific Computing*. Cambridge University Press, second edition.
- Reagan, J. A., McCormick, M. P., and Spinhirne, J. D. (1989). Lidar sensing of aerosols and clouds in the troposphere and stratosphere. *Proceedings of the IEEE*, 77(3):433–448.
- Riley, K., Hobson, M., and Bence, S. (1998). *Mathematical methods for physics and engineering*, pages 1187 – 1189. Cambridge University Press, third edition.
- Rodgers, C. D. (2000). *Inverse methods for atmospheric sounding: Theory and practice*, volume 2 of *Series on Atmospheric, Oceanic, and Planetary Physics*. World Scientific, Singapore, second edition.

- Russell, P. B., Swissler, T. J., and McCormick, M. P. (1979). Methodology for error analysis and simulation of lidar aerosol measurements. *Applied Optics*, 18(22):3783–3796.
- Science and Technology Facilities Council (STFC) [Wrench, C.L.] (2006 – 2011). Chilbolton Facility for Atmospheric and Radio Research (CFARR) data. Available from NCAS British Atmospheric Data Centre at http://badc.nerc.ac.uk/view/badc.nerc.ac.uk_ATOM_dataent_chobs.
- Shcherbakov, V. (2007). Regularized algorithm for Raman lidar data processing. *Applied Optics*, 46(22):4879–4889.
- Sherlock, V., Hauchecorne, A., and Lenoble, J. (1999). Methodology for the independent calibration of Raman backscatter water-vapor lidar systems. *Applied Optics*, 38(27):5816–5837.
- Turner, D. D., Ferrare, R. A., Brasseur, L. A. H., and Feltz, W. F. (2002). Automated retrievals of water vapor and aerosol profiles from an operational Raman lidar. *Journal of Atmospheric and Oceanic Technology*, 19(1):37–50.
- UK Meteorological Office [Parton, G.] (2006 – 2011). Met Office Global Radiosonde Data. Available from the NCAS British Atmospheric Data Centre at http://badc.nerc.ac.uk/view/badc.nerc.ac.uk_ATOM_dataent_GLOBRADS.
- Vaughan, M., Young, S., Winker, D., Powell, K., Omar, A., Liu, Z. Y., Hu, Y. X., and Hostetler, C. (2004). Fully automated analysis of space-based lidar data: an overview of the CALIPSO retrieval algorithms and data products. *Laser Radar Techniques for Atmospheric Sensing*, 5575:16–30.
- Velotta, R., Bartoli, B., Capobianco, R., Fiorani, L., and Spinelli, N. (1998). Analysis of the receiver response in lidar measurements. *Applied Optics*, 37(30):6999–7007.
- Volkov, S. N., Kaul, B. V., and Shelefontuk, D. I. (2002). Optimal method of linear regression in laser remote sensing. *Applied Optics*, 41(24):5078–5083.
- Wandinger, U. and Ansmann, A. (2002). Experimental determination of the lidar overlap profile with Raman lidar. *Applied Optics*, 41(3):511–514.
- Whiteman, D. N. (1999). Application of statistical methods to the determination of slope in lidar data. *Applied Optics*, 38(15):3360–3369.
- Whiteman, D. N. (2003). Examination of the traditional Raman lidar technique. I. Evaluating the temperature-dependent lidar equations. *Applied Optics*, 42(15):2571–2592.
- Wiegner, M., Emeis, S., Freudenthaler, V., Heese, B., Junkermann, W., Munkel, C., Schafer, K., Seefeldner, M., and Vogt, S. (2006). Mixing layer height over Munich, Germany: Variability and comparisons of different methodologies. *Journal of Geophysical Research — Atmospheres*, 111(D13):17.
- Woodhouse, I. and Agnew, J. (2010 – 2011). Chilbolton AERONET Level 1.0 real time data. Available from NASA GSFC at <http://aeronet.gsfc.nasa.gov>.